

Article

Analysis and Optimization of a Novel Compact Compliant 2-DOF Positioner for Positioning to Assess Bio-Specimen Characteristics

Minh Phung Dang ^{1,*}, Hieu Giang Le ¹, Chi Thien Tran ¹, Vo Duc Trieu Nguyen ¹ and Ngoc Le Chau ²

¹ Faculty of Mechanical Engineering, Ho Chi Minh City University of Technology and Education, Ho Chi Minh City 700000, Vietnam

² Faculty of Mechanical Engineering, Industrial University of Ho Chi Minh City, Ho Chi Minh City 700000, Vietnam

* Correspondence: phungdm@hcmute.edu.vn

Abstract: A novel compact 2-DOF compliant positioner is developed for the purpose of achieving good characteristics such as high natural frequency, high displacement amplification ratio, good linear motion, and compact structure based on its symmetrical structure. To be specific, the developed stage is proposed according to an advanced six-lever displacement amplifier arranged at an inclination angle of the rigid bar utilizing right circular hinges and a parallel guiding mechanism with integrated flexure leaf hinges to attain the above-mentioned characteristics and reduce the decoupling mobility error. First, to quickly assess the initial quality response, an integration method of kinetostatic analysis, the Lagrange method, and finite element analysis was applied to evaluate and verify the quality characteristic of the stage. The experimental result showed that the error between the analytical method and the FEA method was 1.3%, which was relatively small and reliable for quickly assessing the primary quality response of the proposed positioner. Next, to boost the important output characteristics of the developed positioner, the integration approach of the response surface method and NSGA-II algorithm was utilized to find the optimal design variables. Finally, a prototype was manufactured based on the CNC milling method to validate the experimental and FEA analysis results. The attained results show that the optimal results of safety factor and output displacement were 2.4025 and 248.9 μm . Moreover, the FEA verification results were 2.4989 and 242.16 μm , with errors for safety factor and output displacement between the optimal result and the FEA result of 3.86% and 2.78%, respectively. In addition, the simulation and experimental results of the first natural frequency were 371.83 Hz and 329.59 Hz, respectively, and the error between the FEA result and experimental result for the first natural frequency was 11.36%. Furthermore, the achieved results show that the relationship between input displacement and output displacement of the experimental result and the FEA result of the developed structure achieved a good linear connection. These results suggest that the proposed positioner will be a potential structure employed in precise positioning systems and nanoindentation testing positioning systems for checking bio-specimens' behaviors.

Keywords: flexure-based mechanism; 2-DOF compliant positioner; response surface method; kinetostatic analysis; NSGA-II



Citation: Dang, M.P.; Le, H.G.; Tran, C.T.; Nguyen, V.D.T.; Chau, N.L. Analysis and Optimization of a Novel Compact Compliant 2-DOF Positioner for Positioning to Assess Bio-Specimen Characteristics. *Machines* **2024**, *12*, 421. <https://doi.org/10.3390/machines12060421>

Academic Editor: Dan Zhang

Received: 23 April 2024

Revised: 4 June 2024

Accepted: 11 June 2024

Published: 19 June 2024



Copyright: © 2024 by the authors. Licensee MDPI, Basel, Switzerland. This article is an open access article distributed under the terms and conditions of the Creative Commons Attribution (CC BY) license (<https://creativecommons.org/licenses/by/4.0/>).

1. Introduction and Motivation

The nanoindentation testing equipment is designed to accurately assess hardness, elastic modulus, and creep by applying tiny loads and measuring depths at the nanoscale. This technique can be employed to observe and analyze the properties of organic, inorganic, rigid, and soft materials [1]. The development of compact-size mechanical mechanisms with improved performances has sparked significant interest because of advancements in in-situ nanoindentation testers. The objectives of compact-sized mechanisms are to achieve a low weight and no assembly, allowing them to be integrated into nanoindentation devices

for real-time observation of the mechanical properties of a material sample [2,3]. In addition, in-situ nanoindentation testing is particularly important for examining the properties of bio-specimens used in implants, such as bone, tooth, femur, and prosthesis [4].

Currently, the positioning stage of the nanoindentation testing method relies on conventional technologies such as servo motors, gears, sliding rails, ball screws, and rigid hinges. With such traditional applications, it is challenging to attain precise positioning due to the adverse effects of backlash, friction, and wear. Thus, a highly accurate locating platform is crucial for the indentation procedure to precisely determine the location before assessing the features of the material specimen. Compliant mechanisms have been extensively utilized to address the drawbacks of conventional technologies due to their inherent advantages, including the absence of wear, backlash, friction, and lubrication, as well as achieving cost-effectiveness and compactness [5–7]. Generally, there are two main mechanisms in a typical in-situ nanoindentation system. Specifically, a fine 01-dof stage is responsible for positioning the indenter, and a fine 02-dof stage is used to position the specimen precisely before conducting a nanoindentation testing process to check the characteristics of the bio-specimen [8].

Regarding the above-mentioned considerations, numerous researchers have made noteworthy advancements in constructing mechanical platforms for the purpose of in-situ nanoindentation. Particularly, Rabe et al. created a small and flexible 01-dof positioner. This positioner was integrated into an in-situ nanoscratch device to test the mechanical properties of material samples [9]. Huang et al. developed a flexible 01-dof positioner using a flexure half-bridge displacement amplifier to control the indenter used in the in-situ nanoindentation device [10]. Furthermore, Huang et al. created a flexible 01-dof positioner. The positioner included a flexure one-lever displacement amplifier integrated with elliptical compliant hinges. This device tests the indentation response of single-crystal silicon [11]. Dang et al. proposed a flexure 01-dof platform for guiding the indenter to check mechanical characteristics in the nanoindentation testing system [12]. In addition, Huang et al. developed a nanoindentation testing system including an XY stage with a working stroke of $12 \times 12 \mu\text{m}$ and a compliant Z-stage of $40 \mu\text{m}$ [13].

Numerous XY stages with differential structures have been created for micro/nano-positioning systems. Among these types of applications, a piezoelectric actuator (PEA) is frequently selected because of its exceptional accuracy and rapid reaction time. However, a disadvantage of the PEAs is their restricted output stroke [14]. This results in a constraint that negatively affects the achievement of a significant output displacement for the compliant stages. Consequently, a number of displacement amplifiers were created to enhance the output displacement of developed mechanisms, such as an L-shape lever [15], a hybrid rhombus lever [16], a double lever [17], a single lever [18], a symmetric four-lever [19], a hybrid bridge-lever-bridge [20], and a hybrid bridge-Scott-Russell mechanism [21].

Several research groups have mostly concentrated on designing compliant XY stages by building series-parallel kinematic chains in conjunction with PEAs to achieve superior performances. Specifically, Gu et al. applied the compliance matrix method to model the resonant frequency of a proposed positioner for vibration-assisted polishing [22]. Ling et al. applied the pseudo-static model method to analyze a dynamic characteristic of the proposed XY stage for an accurate positioning system [16]. Wu et al. applied the kinetostatics calculation method to model the dynamic characteristics of a proposed XY stage for a precise positioning system [23].

In recent years, several researchers have concentrated on incorporating displacement amplifiers into compliant positioning stages to increase the working stroke of a precise positioning system. For example, Wu et al. developed a four-lever displacement amplifier utilizing right circular hinges integrated into a compliant XY positioner for a precise positioning system [23]. Gang et al. applied a bridge displacement amplifier using flexure leaf hinges incorporated into an XY stage for a precise positioning system [24]. Zhu et al. introduced a symmetrical Scott–Russell displacement amplification mechanism that was integrated into an XY stage for application in a highly accurate positioning system [25].

Ding et al. utilized a one-lever displacement amplifier integrated into the 03-dof stage which could be applied for micro–nano manipulation [26]. However, little attention has been paid to a flexure XY positioner that employs an advanced symmetrical six-lever displacement amplifier arranged at an inclination angle of the rigid bar integrated right circular hinges and parallel guiding mechanism integrated flexure leaf hinges. Possibly, this positioner can contribute to the achievement of a compact structure, a high displacement amplification ratio, and a good linear relationship between input displacement and output displacement for nanoindentation testing devices.

For years, the Taguchi method (TM) has been widely used in engineering for analysis and optimization. The TM proves to be the most appropriate technique as it requires fewer experiments than many other techniques. Nevertheless, as the TM only improves one specific factor, it must be combined with various methods to enhance several responses. Numerous studies have been conducted to integrate optimization algorithms and combine various optimization approaches. For example, Dang et al. devised a method that combines TM, fuzzy logic and the moth–flame optimization algorithm to enhance the output characteristics of the compliant joint [27]. Dao utilized a combination of the Taguchi technique and Cuckoo search algorithm to maximize the overall output responses of a flexure positioner [28]. Although these combined methods can address the TM’s weakness in improving only one factor, they are not efficient in developing a new design as it is time-consuming for designers to develop a new product. Instead, they work better in the field of experimental optimization research. Consequently, this study aimed at devising a hybrid method that can address a multi-objective optimization issue and save time for users. Specifically, the proposed method integrates the response surface method (RSM) [29], which can calculate the regression equations, and the Nondominated Sorting Genetic Algorithm II (NSGA-II) [30,31], which can optimize problems with multiple criteria.

The primary objective of this study is to develop a new flexible 02-dof positioner that is combined with an advanced symmetrical six-lever displacement amplifier and parallel mechanism to achieve good quality characteristics. The research started with the resonance frequency of the developed positioner being assessed and confirmed by the elastic beam theory, Lagrange technique, and FEA analysis. It was essential to achieve optimal parameters for both the output displacement and the safety factor, but these quality responses disagreed. A possible solution was to use a multi-criteria optimization strategy to simultaneously attain a high safety factor and a significant output displacement with the frequency limitation constraint. Therefore, this study employed a hybrid technique that combined RSM and the NSGA-II algorithm integrated into Ansys Workbench to optimize the key parameters for improving quality responses, including the safety factor and output displacement. The optimization was performed in the condition where the resonant frequency limitation was met. Finally, a prototype was fabricated to confirm the optimal outcomes and FEA analysis results. Unlike previous studies that utilized the wire electric discharge machining process to manufacture the compliant positioning stages [11,23], this study employed a computerized numerical control milling process with a small endmill tool to fabricate the suggested prototype. Specially, this fabrication approach was chosen to improve both the fabrication precision and the quality of the manufactured surfaces. Figure 1 demonstrates the promising use of the developed platform to accurately situate the bio-specimen in the nanoindentation testing equipment.

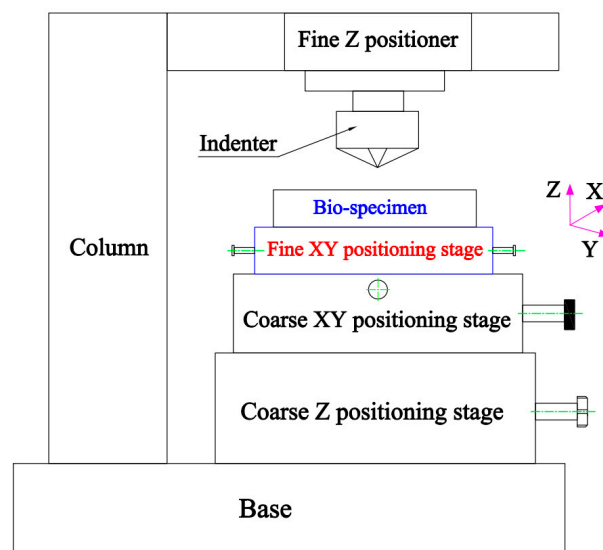


Figure 1. Bench for conducting nanoindentation tests.

2. Mechanical Compliant XY Positioner Design

This section presents the development of a novel design for the compliant XY positioner, which aims to achieve a high natural frequency, a high displacement amplification ratio, a small parasitic motion error, a linear relationship of input displacement and output displacement, and a compact structure. The developed positioner is intended to apply for an accurate positioning system and nanoindentation testing positioning system for locating to check the characteristics of bio-specimen. To accomplish these above-mentioned goals, a novel positioner is created according to the PEAs, symmetrical structure, and parallel guiding mechanism, as well as a AL7075 material. However, the PEAs' working travel is restricted. Therefore, to enhance the working stroke and achieve a good linear relationship between the proposed positioner's input and output displacement, an advanced six-lever displacement amplifier (ASDA) was developed for integration into the proposed positioner, as illustrated in Figure 2. Moreover, to attain a compact structure, high first natural frequency, and large displacement amplification ratio, as well as to decrease the decoupling mobility error, the proposed structure (illustrated in Figure 3) comprised an ASDA arranged at an inclination angle of the rigid bars and utilized right circular hinges and a parallel guiding mechanism integrated with flexure leaf hinges. The chosen material for constructing this recommended positioner was AL7075 because of its excellent properties, such as a Young modulus of 71.7 GPa, a Poisson ratio of 0.33, and a high yield strength of 503 MPa. Regarding its design, this mechanism included the following main components: (i) twenty-eight fixed holes were employed for connecting with an intermediate plate to evaluate the quality responses; (ii) a piezo actuator and translational screw were used to generate input displacement and measure the first natural frequency based on the PEA actuator; and (iii) the intermediate plate was fixed on an un-vibration table to fix the proposed prototype and ensure reliable measurement results. Figure 4a,b illustrate the 2D layout and 3D model of the proposed assembly structure. To achieve a good initial design, a total dimension of the proposed stage was limited, and the values of the main dimensions and the range of design variables were developed according to designer experience and the machining conditions of the proposed fabricating method. Later, the initial design of the proposed positioner was investigated by FEM to achieve a good design. Next, an optimization process was conducted to enhance the quality responses in next sections. Specially, Figure 5 presents the design diagram for determining the proposed platform's main parameters and design variables, and Table 1 depicts the main dimension values of the proposed stage. The total compact dimensions of the proposed 02-dof positioner were $228 \times 228 \times 10$ (mm), as illustrated in Figure 5 and Table 1.

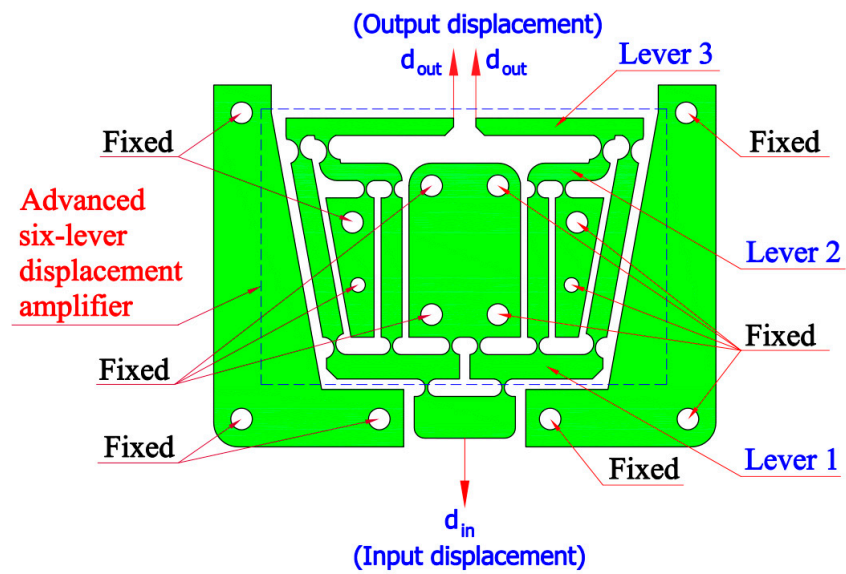


Figure 2. Structure of an advanced six-lever displacement amplifier.

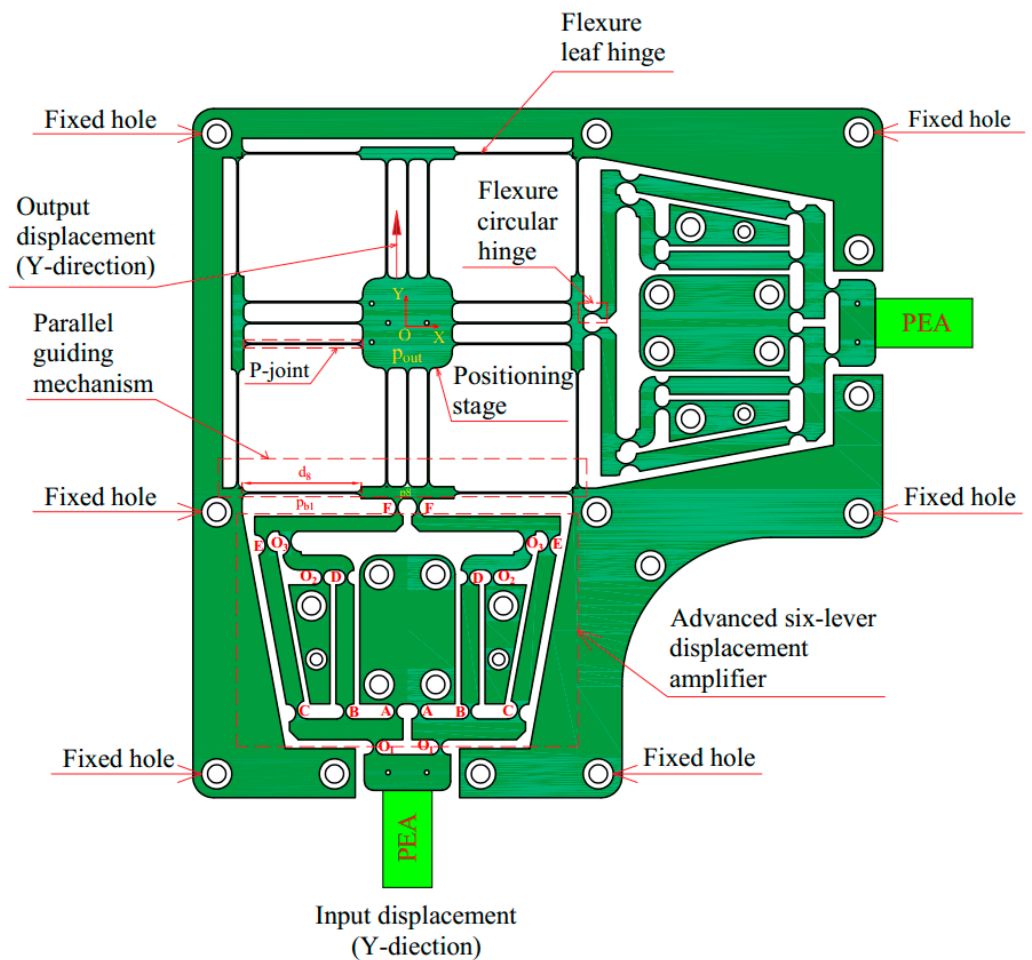
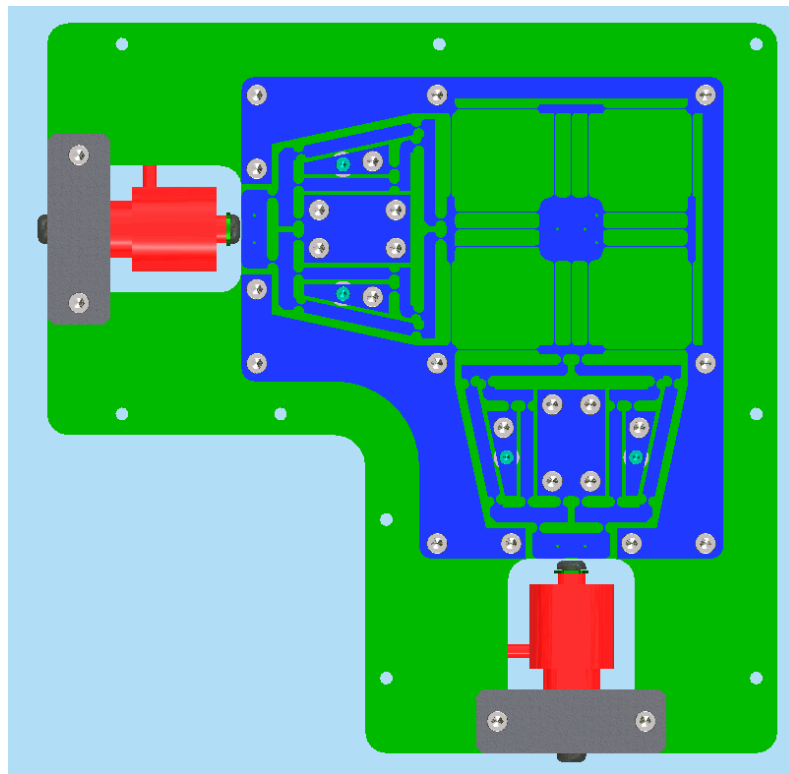
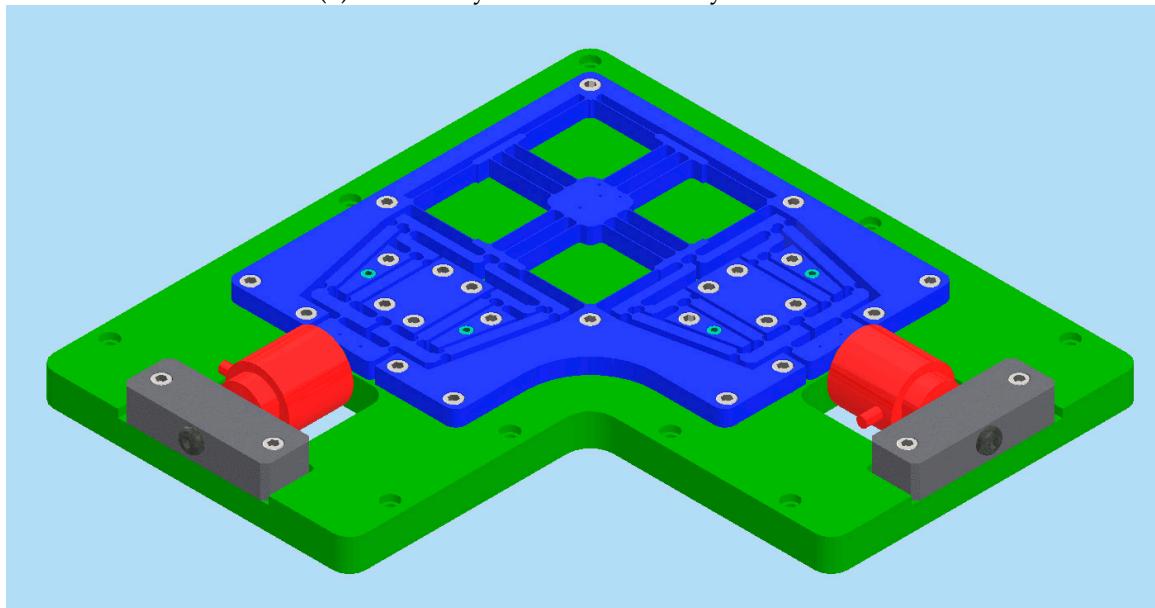


Figure 3. Structure of proposed compliant 2-DOF positioner.



(a) The 2D layout of the assembly structure.



(b) The 3D layout of the assembly structure.

Figure 4. The proposed assembly design structure: (a) 2D layout design, (b) 3D model design.

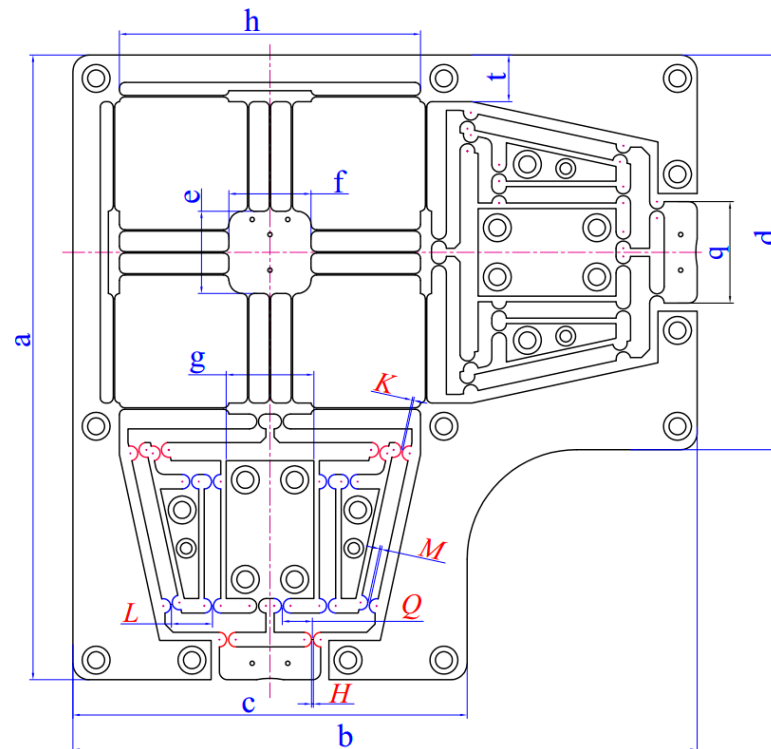


Figure 5. Main dimensions and design variables of the proposed platform.

Table 1. Key considerations influencing the developed positioner.

Symbol	Value (mm)	Symbol	Value (mm)
a	228	h	110
b	228	q	37
c	144	K	$0.5 < K < 0.6$
d	144	M	$0.53 < M < 0.65$
e	30	H	$0.62 < H < 0.74$
f	30	Q	$7.2 < Q < 12$
g	30	L	$15 < L < 18$
t	17		

3. Proposed Method for Modeling and Optimization of Compliant XY Positioner

This section outlines the suggested method for modeling and optimizing the flexure 2-DOF positioner. The proposed strategy is formulated according to a metaheuristic algorithm and analytical approach. The present research combines the principles of the elastic beam theory [23] and the Lagrange technique to construct the kinetostatic and dynamic calculations for the compliant 2-dof positioner. Firstly, the primary natural frequency of the XY positioner was promptly assessed using the elastic beam theory and the Lagrange technique. Next, finite element analysis was conducted to confirm the first natural frequency's analytical result. Then, the integration method of the RSM and NSGA-II algorithm was utilized to optimize the positioner's key parameters to enhance the safety factor and output displacement with the frequency constraint. Further details about the process of modeling and optimizing for the proposed positioner are presented in the flowchart of the hybrid framework strategy (Figure 6). Additional details about the NSGA-II algorithm can be found in refs. [30,31].

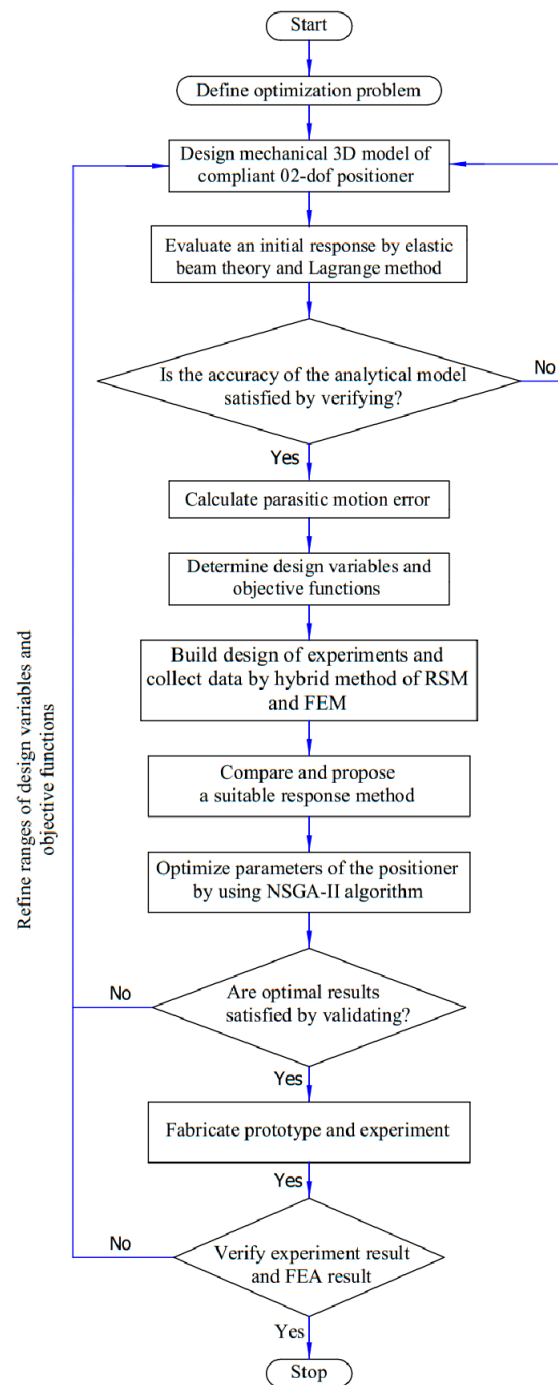


Figure 6. The flowchart of combination optimization methodology for the proposed positioner.

The hybrid methodology was executed with the following steps:

- Step 1: Determine the optimization problem;
- Step 2: Design a mechanical 3D model for the proposed stage and evaluate the initial quality characteristics using the elastic beam theory and Lagrange method;
- Step 3: Verify the analytical result through FEA analysis;
- Step 4: Evaluate the decoupling mobility error with FEM;
- Step 5: Determine design variables and objective functions;
- Step 6: Collect data using the response surface method to build the design of numerical experiments. The central composite design is utilized to set the number of experiments, which depends on several design variables;

Step 7: Compare and offer a suitable response surface kind to achieve the best goodness of fit diagram for mapping input parameters and output responses;

Step 8: Optimize the main parameters of the proposed stage using the NGA-II algorithm integrated into the Ansys workbench to enhance the quality responses of the developed positioner;

Step 9: Fabricate the prototype of the developed positioner and conduct experiments to measure important responses of the positioner, including first natural frequency, output displacement, and the relationship between input displacement and output displacement;

Step 10: Verify optimal results via FEA analysis and experimental results.

4. Results and Discussion

4.1. Modeling of Kinetostatics

The proposed positioner was designed for use in positioning tasks to assess the behaviors of bio-specimens, as well as in precise positioning systems. The main responses of compliant positioners include the high first natural frequency, high output displacement, and high safety factor. Therefore, first, the initial natural frequency of the developed platform was assessed via the analytical method of elastic beam theory and the Lagrange method. In addition, a half displacement amplification mechanism was used to investigate the output response of the proposed positioner due to symmetrical configuration. Figure 3 depicts the diagram for the advanced six-lever displacement amplifier arranged at an angle of inclination of the rigid bar. This amplifier comprises three floors of lever displacement amplification mechanism (LAM), namely, LAM 1, LAM 2, and LAM 3, arranged in a parallel structure. Furthermore, the dimensions of the lever lengths ($d_1, d_2, d_3, d_4, d_5, d_6,$ and d_7) and the rotary centers ($O_1, O_2,$ and O_3) are illustrated in Figure 7.

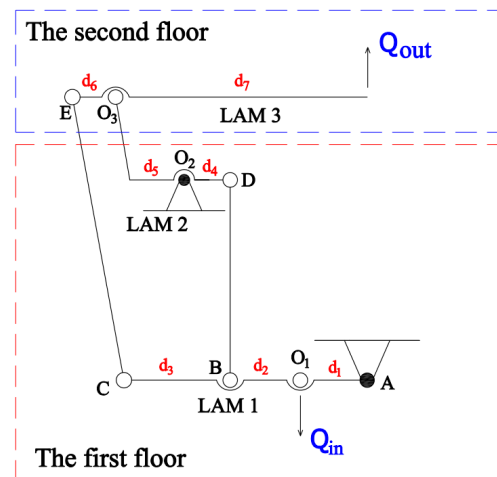


Figure 7. Diagram of advanced six-lever displacement amplification mechanism.

The report continues with the process of formulating equations and calculation of different components. First, this study investigates the input stiffness of the suggested structure. To be more precise, the calculation of stiffness for a flexure right circular hinge involves three components. The bending rigidity (K_B^{rc}) is determined by the diagonal force, the rotation rigidity (K_T^{rc}) is influenced by the moment, and the linear stiffness (K_L^{rc}) is affected by the axial force. Correspondingly, for the stiffness calculation of a compliant leaf hinge, rotation and linear rigidities are indicated by K_T^l and K_L^l , correspondingly. In addition, Figure 8 shows a simplified construction plot of a compliant right circular hinge and key factors, including the thickness, the length, and the width. Equations (1)–(3) are employed for calculating the stiffness values of the right circular hinge.

$$K_B^{rc} = \frac{2Ewu^{2.5}}{9\pi r^{0.5}}, \quad (1)$$

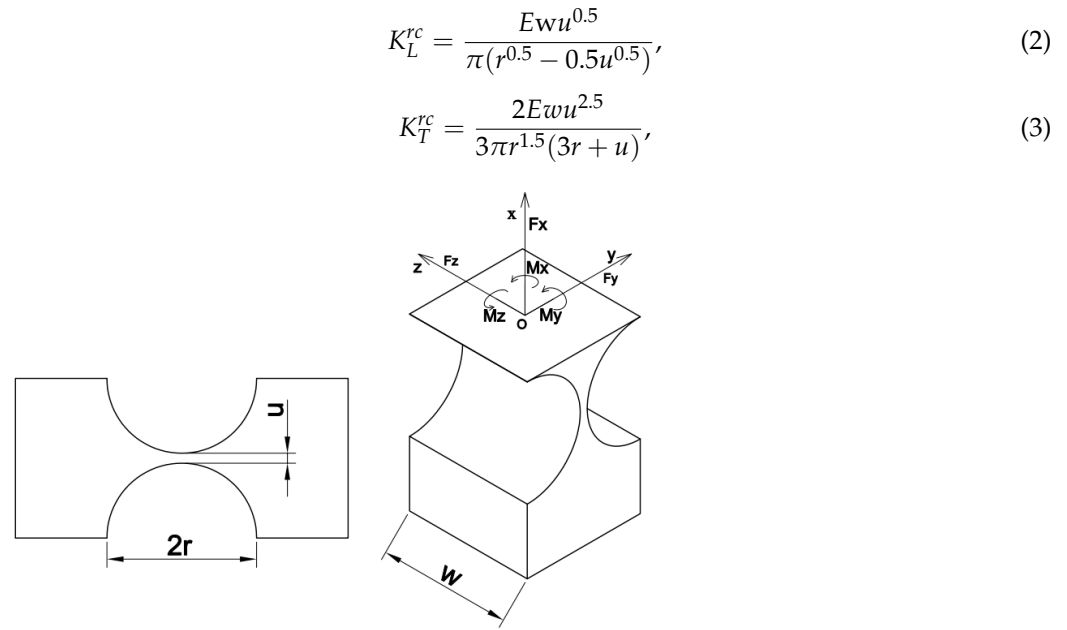


Figure 8. Geometrical specifications of a right circular hinge.

Figure 9 is a simplified diagram illustrating the construction of a compliant rectangular hinge. Moreover, the crucial parameters, including thickness, length, and width, are demonstrated in alignment with the force and torque operating on the flexible rectangular joint. Equations (4)–(6) are used to compute the stiffness values of the leaf hinge.

$$K_T^l = \frac{Ewa^3}{12d}, \tag{4}$$

$$K_L^l = \frac{Ewa}{d}, \tag{5}$$

$$M_T^l = K_T^l \Delta\alpha, \tag{6}$$

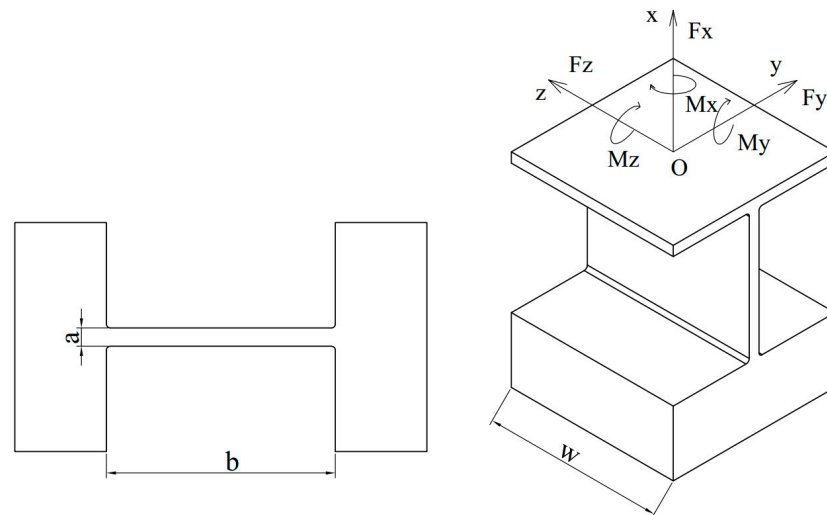


Figure 9. Geometrical specifications of a compliant rectangular hinge.

Figure 10 illustrates the initial and ongoing conditions of ASDA. To be more precise, the displacement of the multistage lever causes deformation angles that help to visually represent the different levels of distortion in the mechanism during its operation.

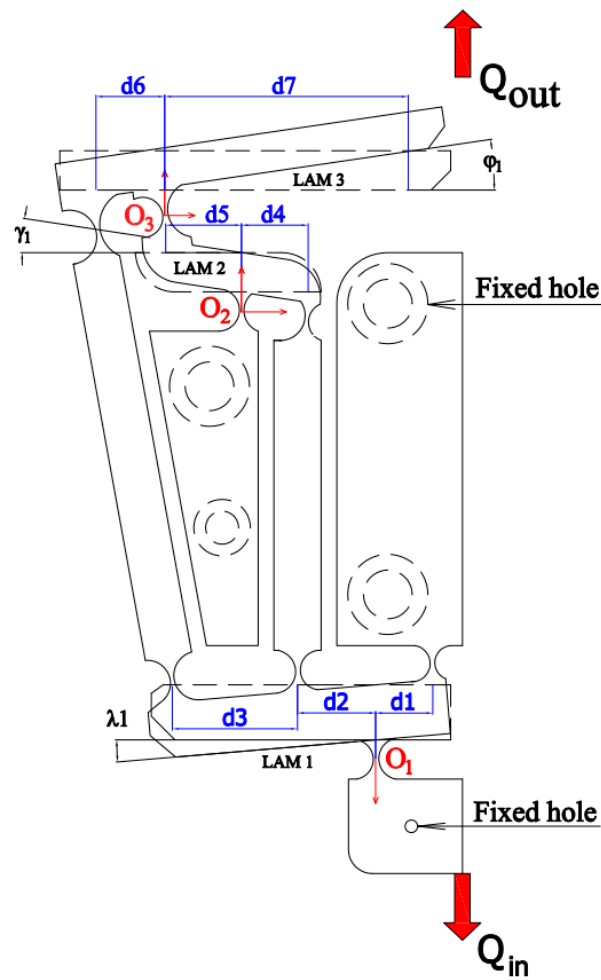


Figure 10. Diagram demonstrating the relationship between force and deformation in one part of the ASDA.

The force analysis diagrams for lever beams 1–3 of developed displacement amplifier are illustrated in Figures 11–13.

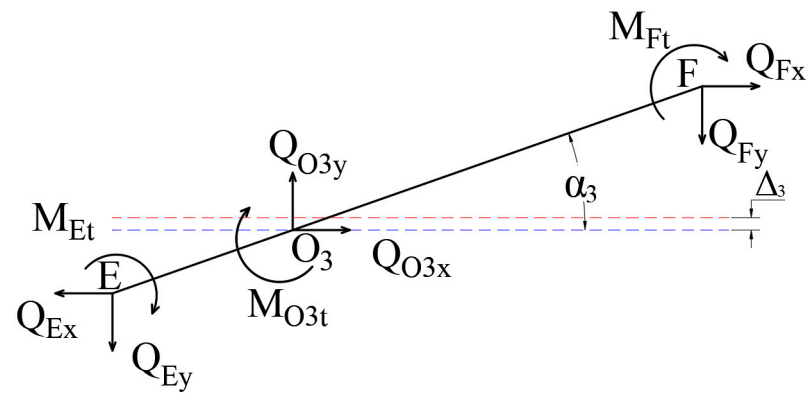


Figure 11. Beam 3's force investigation schema.

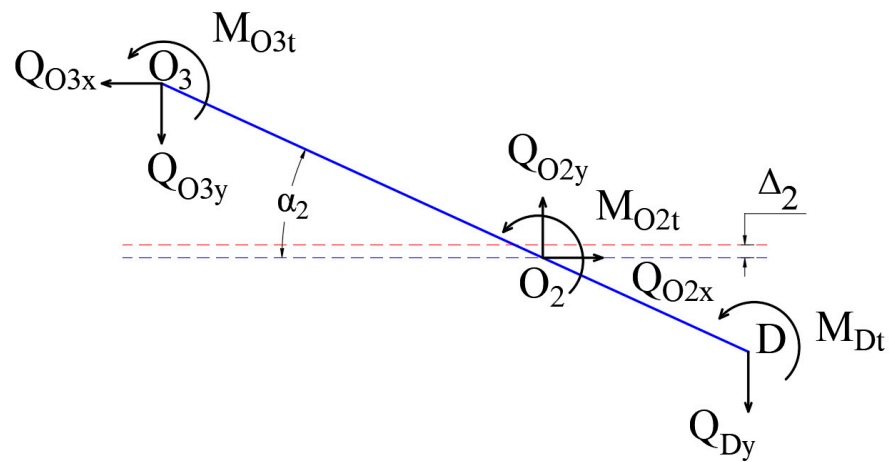


Figure 12. Force examination schema of 2nd beam.

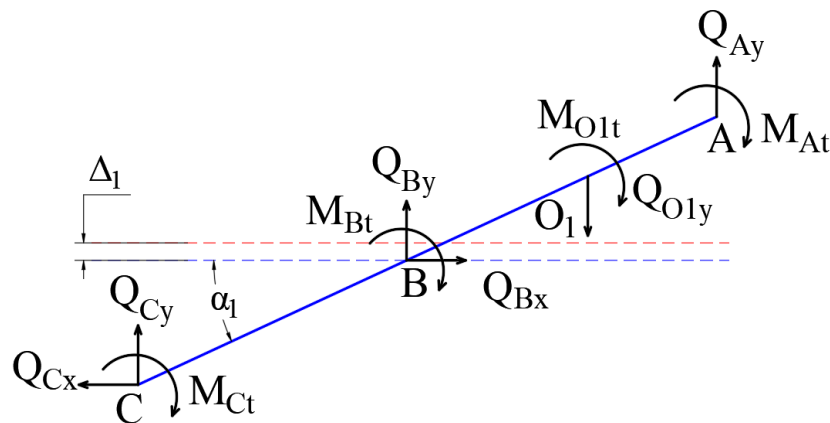


Figure 13. Force investigation schema of 1st beam.

To calculate the force equilibrium equations for beam 3, we used the following formulas:

$$Q_{O3y} = Q_{Ey} + Q_{Fy} \tag{7}$$

$$Q_{Ey}d_6 = Q_{Fy}d_7 + M_{Et} + M_{O3t} + M_{Ft} \tag{8}$$

The bending moments at points E , O_3 , and F are denoted as M_{Et} , M_{O3t} , and M_{Ft} , correspondingly. Three forces, denoted as Q_{Ey} , Q_{O3y} , and Q_{Fy} , are applied at points E , O_3 , and F , correspondingly, in the y -axis direction during the operation of the structure. In addition, the deformation value at point F is the sum of two deformations: the deformation caused by the joints at O_3 revolving around its axis ($d_7\alpha_3$) and the deformation caused by drift (Δ_3). Moreover, the forces Q_{O3y} and Q_{Fy} can be derived by multiplying stiffness and displacement. The calculations are determined using the following equations:

$$Q_{O3y} = K_{O3x}\Delta_3 \tag{9}$$

$$Q_{Fy} = K_{Fy}(d_7\alpha_3 - \Delta_3) \tag{10}$$

$$M_{O3t} = K_{O3t}\alpha_3 \tag{11}$$

$$M_{Ft} = K_{Ft}\alpha_3 \tag{12}$$

$$M_{Et} = K_{Et}\alpha_3 \tag{13}$$

More precisely, K_{O3x} represents the resistance to lateral bending through the force Q_{O3y} , while K_{Fy} refers to the output stiffness of the ASDA at point F . Additionally, the

rotational stiffnesses K_{O3t} , K_{Ft} , K_{Et} represent the stiffness of the flexure hinges at positions O_3 , F , and E , respectively.

By substituting Equations (9) and (10) into Equation (7), the resulting outcomes are obtained as follows:

$$K_{O3x}\Delta_3 = Q_{Ey} + K_{Fy}(d_7\alpha_3 - \Delta_3) \quad (14)$$

$$\Rightarrow \Delta_3 = \frac{Q_{Ey} + K_{Fy}d_7\alpha_3}{K_{O3x} + K_{Fy}} \quad (15)$$

Replacing Equations (10)–(13) into (8), the consequences are achieved as the following equations.

$$Q_{Ey}d_6 = K_{Fy}d_7(d_7\alpha_3 - \Delta_3) + K_{Et}\alpha_3 + K_{O3t}\alpha_3 + K_{Ft}\alpha_3 \quad (16)$$

$$\Rightarrow \alpha_3 = \frac{Q_{Ey}d_6(K_{O3x} + K_{Ey}) + Q_{Ey}K_{Fy}d_7}{(K_{O3x} + K_{Fy})(K_{Fy}d_7^2 + K_{Et} + K_{O3t} + K_{Ft}) - K_{Fy}^2d_7^2} \quad (17)$$

$$\Delta_3 = \frac{Q_{Ey} + Q_{Ey}K_{Fy}d_7[d_6(K_{O3x} + K_{Fy}) + K_{Fy}d_7] / [(K_{O3x} + K_{Fy})(K_{Fy}d_7^2 + K_{Et} + K_{O3t} + K_{Ft}) - K_{Fy}^2d_7^2]}{(K_{O3x} + K_{Fy})} \quad (18)$$

$$\Delta_3 = \frac{K_{Fy}d_7^2 + K_{Et} + K_{O3t} + K_{Ft} + K_{Ey}d_7d_6}{(K_{O3x} + K_{Fy})(K_{Fy}d_7^2 + K_{Et} + K_{O3t} + K_{Ft}) - K_{Fy}^2d_7^2} Q_{Ey} \quad (19)$$

In addition, the displacement amplification proportion of beam 3 is determined by the following equation:

$$\mu_3 = \frac{(d_7 + d_6)\alpha_3 - \Delta_3}{d_6\alpha_3 + \Delta_3} \quad (20)$$

$$K_{in3} = \frac{Q_{Ey}}{d_6\alpha_3 + \Delta_3} \quad (21)$$

Based on the force examination schema of lever 2, as illustrated in Figure 11, the force–balance calculations are established by the following Equations (22) and (23):

$$Q_{O2y} = Q_{O3y} + Q_{Dy} \quad (22)$$

$$Q_{Dy}d_4 = Q_{O3y}d_5 + M_{O3t} + M_{O2t} + M_{Dt} \quad (23)$$

The bending moments at locations O_3 , O_2 , and D are denoted as M_{O3t} , M_{O2t} , and M_{Dt} , respectively. Three forces, Q_{Dy} , Q_{O2y} , and Q_{O3y} , are exerted at points D , O_2 , and O_3 , respectively, in the y -axis direction through the operation of the mechanism.

Moreover, the deformation at point O_3 is an integration of two deformations: the deformation produced by joints at O_2 revolving about its axis $(d_5 + d_6)\alpha_2$ and the displacement based on drift (Δ_2) .

$$Q_{O2y} = K_{O2x}\Delta_2 \quad (24)$$

$$Q_{O3y} = K_3(d_5\alpha_2 - \Delta_2) \quad (25)$$

$$M_{O3t} = K_{O3t}\alpha_2 \quad (26)$$

$$M_{O2t} = K_{O2t}\alpha_2 \quad (27)$$

$$M_{Dt} = K_{Dt}\alpha_2 \quad (28)$$

The lateral bending stiffness, denoted as K_{O2x} , is determined by the force Q_{O2y} . On the other hand, the rotary stiffness at the D point is represented by K_{Dt} . By substituting Equations (24) and (25) into Equation (22), we obtain the following calculations.

$$K_{O2x}\Delta_2 = Q_{Dy} + K_{in3}(d_5\alpha_2 - \Delta_2) \quad (29)$$

$$\Rightarrow \Delta_2 = \frac{Q_{Dy} + K_{in3}d_5\alpha_2}{K_{O2x} + K_{in3}} \quad (30)$$

Replacing (25)–(28) into (23), the consequences are achieved.

$$Q_{Dy}d_4 = K_{in3}d_5(d_5\alpha_2 - \Delta_2) + K_{O3t}\alpha_2 + K_{O2t}\alpha_2 + K_{Dt}\alpha_2 \quad (31)$$

$$\Rightarrow \alpha_2 = \frac{Q_{Dy}d_4(K_{O2x} + K_{in3}) + K_{in3}d_5Q_{Dy}}{(K_{O2x} + K_{in3})(K_{in3}d_5^2 + K_{O3t} + K_{O2t} + K_{Dt}) - K_{in3}^2d_5^2} \quad (32)$$

$$\Delta_2 = \frac{K_{in3}d_5^2 + K_{O3t} + K_{O2t} + K_{Dt} + K_{in3}d_5d_4}{(K_{O2x} + K_{in3})(K_{in3}d_5^2 + K_{O3t} + K_{O2t} + K_{Dt}) - K_{in3}^2d_5^2} Q_{Dy} \quad (33)$$

Regarding beam 2, the amplification proportion and the input stiffness are defined by the following equations:

$$\mu_2 = \frac{d_5\alpha_2 - \Delta_2}{d_4\alpha_2 + \Delta_2} \quad (34)$$

$$K_{in2} = \frac{Q_{Dy}}{d_4\alpha_2 + \Delta_2} \quad (35)$$

Based on the force examination schema of beam 1, the force–balance equations can be established as the following Equations (36) and (37).

$$Q_{O1y} = Q_{Cy} + Q_{By} + Q_{Ay} \quad (36)$$

$$Q_{O1y}d_1 = Q_{Cy}(d_1 + d_2 + d_3) + Q_{By}(d_1 + d_2) + M_{Ct} + M_{Bt} + M_{O1t} \quad (37)$$

Particularly, the bending moments of the points *C*, *B*, *A*, and *O*₁ are represented as M_{Ct} , M_{Bt} , M_{At} , and M_{O1t} , respectively. Four forces, Q_{Ay} , Q_{Cy} , Q_{By} , and Q_{O1y} , are performing at points *A*, *C*, *B*, and *O*₁ according to the *y*-direction when the mechanism works, correspondingly. The deformation at location *C* is an integration of two deformations: the deformation produced by joints at *O*₁ revolving around their axis $(d_1 + d_2 + d_3)\alpha_1$ and the displacement caused by drift (Δ_1).

$$Q_{Ay} = K_{Ax}\Delta_1 \quad (38)$$

$$Q_{Cy} = K_1[(d_1 + d_2 + d_3)\alpha_1 + \Delta_1] \quad (39)$$

$$Q_{By} = K_2[(d_1 + d_2)\alpha_1 + \Delta_1] \quad (40)$$

$$M_{Ct} = K_{Ct}\alpha_1 \quad (41)$$

$$M_{Bt} = K_{Bt}\alpha_1 \quad (42)$$

$$M_{O1t} = K_{O1t}\theta_1 \quad (43)$$

$$K_1 = \frac{K_{Cy}K_{in3}}{K_{Cy} + K_{in3}} \quad (44)$$

$$K_2 = \frac{K_{By}K_{in2}}{K_{By} + K_{in2}} \quad (45)$$

Replacing (38)–(43) into (37), the following equations can be achieved:

$$\Rightarrow \alpha_1 = \frac{Q_{O1y}d_1 - K_1\Delta_1(d_1 + d_2 + d_3) - K_2\Delta_1(d_1 + d_2)}{K_1(d_1 + d_2 + d_3)^2 + K_2(d_1 + d_2)^2 + K_{Ct} + K_{Bt} + K_{O1t}} \quad (46)$$

Replacing (38)–(40) into (36), the following equations can be achieved:

$$\Rightarrow \Delta_1 = \frac{\frac{Q_{O1y}d_1[K_1(d_1+d_2+d_3)+K_2(d_1+d_2)]}{K_1(d_1+d_2+d_3)^2+K_2(d_1+d_2)^2+K_{Ct}+K_{Bt}+K_{O1t}} - Q_{O1y}}{-(K_{Ax} + K_1 + K_2) + \frac{[K_1(d_1+d_2+d_3)+K_2(d_1+d_2)]^2}{K_1(d_1+d_2+d_3)^2+K_2(d_1+d_2)^2+K_{Ct}+K_{Bt}+K_{O1t}}} \quad (47)$$

The equations provided express the first beam’s displacement amplification ratio and input stiffness.

$$\mu_1 = \frac{(d_1 + d_2)\alpha_1 - \Delta_1}{d_1\alpha_1 + \Delta_1} \quad (48a)$$

$$\mu'_1 = \frac{(d_1 + d_2 + d_3)\alpha_1 - \Delta_1}{d_1\alpha_1 + \Delta_1} \quad (48b)$$

$$K_{in1} = \frac{Q_{O1y}}{d_1\alpha_1 + \Delta_1} \quad (49)$$

The whole amplification proportion of the advanced displacement amplifier is defined by the following equation:

$$A = \mu_3(\mu_1 \times \mu_2 + \mu'_1) \quad (50)$$

4.2. Dynamic Model Analysis

The resonant frequency is determined using the Lagrange approach, which involves calculating the kinetic energy (T) and potential energy (V). Figure 14 depicts the precise locations of masses p_i in the developed positioner. A mobility categorization stage is utilized to support the determination of the natural frequency of the design based on the location and motion trajectory of the components.

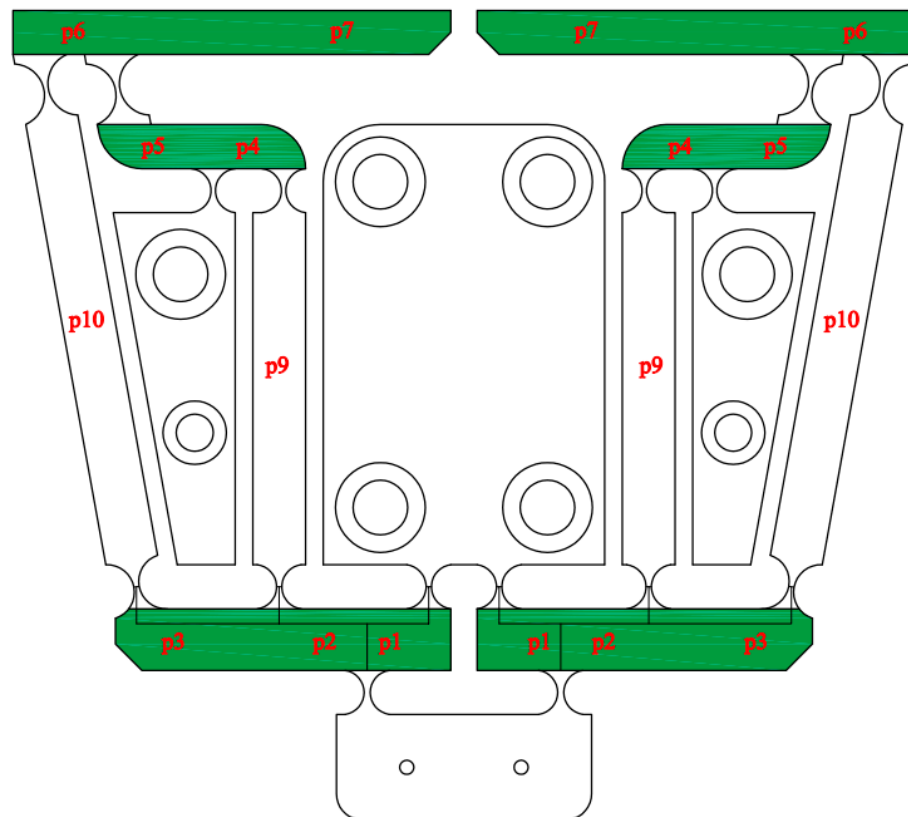


Figure 14. Advanced six-lever amplification mechanism according to symmetrical structure.

The hinges $p_1, p_2, p_3, p_4, p_5, p_6, p_7, p_{b1},$ and p_{b2} symbolize for the rotary and translation motions. In addition, the hinges $p_{in}, p_{out}, p_8, p_9,$ and p_{10} symbolize the transfor-

mations. The kinematic power of the developed positioner can be established using the following equations.

$$T = T_{\eta_1} + T_{\eta_2} \quad (51)$$

$$T_{\eta_1} = T_{\eta_2} = \sum_{i=p_1}^{p_{10}} T_j + \sum_{i=p_{b1}}^{p_{b2}} T_j \quad (52)$$

$$T_{p_{out}} = \frac{1}{2} p_{out} (\eta_1 A)^2 = \frac{p_{out} A^2}{2} \eta_1^2 \quad (53)$$

$$T_{p_{in}} = \frac{p_{in}}{2} \eta_1^2 \quad (54)$$

$$T_{p_8} = \frac{p_8 A^2}{2} \eta_1^2 \quad (55)$$

$$T_{p_9} = \frac{1}{2} 2 p_9 \left(\frac{v \mu_1}{2} \right)^2 = \frac{p_9 \mu_1^2}{4} \eta_1^2 \quad (56)$$

$$T_{p_{10}} = \frac{1}{2} 2 p_{10} \left(\frac{v \mu'_1}{2} \right)^2 = \frac{p_{10} \mu_1'^2}{4} \eta_1^2 \quad (57)$$

$$T_{p_1} = \frac{1}{2} 2 p_1 \left(\frac{v}{2} \right)^2 + \frac{1}{2} 2 \frac{p_1 l_1^2}{3} \left(\frac{v}{2} \right)^2 = \frac{7 p_1}{12} \eta_1^2 \quad (58)$$

$$T_{p_2} = \frac{7 p_2 \lambda_1}{12} \eta_1^2 \quad (59)$$

$$T_{p_3} = \frac{7 p_3 \mu'_1}{12} \eta_1^2 \quad (60)$$

$$T_{p_4} = \frac{7 p_4 \mu'_1}{12} \eta_1^2 \quad (61)$$

$$T_{p_5} = \frac{7 p_5 \mu_2}{12} \eta_1^2 \quad (62)$$

$$T_{p_6} = \frac{7 p_6 A}{12} \eta_1^2 \quad (63)$$

$$T_{p_7} = \frac{7 p_7 A}{12} \eta_1^2 \quad (64)$$

$$T_{p_{b1}} = \frac{1}{2} 8 p_{b1} (vA)^2 + \frac{1}{2} 8 \frac{p_{b1} l_8^2}{3} \left(\frac{vA}{l_8} \right)^2 = \frac{16 p_{b1} A^2}{3} \eta_1^2 \quad (65)$$

$$T_{p_{b2}} = \frac{1}{2} 6 p_{b2} (vA)^2 + \frac{1}{2} 6 \frac{p_{b2} l_9^2}{3} \left(\frac{vA}{l_9} \right)^2 = 4 p_{b2} A^2 \eta_1^2 \quad (66)$$

$$M = p_{out} A^2 + p_{in} + p_8 A^2 + \frac{p_9 \mu_1^2}{2} + \frac{p_{10} \mu_1'^2}{2} + \frac{7}{6} p_1 + \frac{7}{6} p_2 \mu_1^2 + \frac{7}{6} p_3 \mu_1'^2 + \frac{7}{6} p_4 \mu_1^2 + \frac{7}{6} p_5 \mu_2^2 + \frac{7}{6} p_6 A^2 + \frac{7}{6} p_7 A^2 + \frac{32}{3} p_{b1} A^2 + p_{b2} A^2 \quad (67)$$

The positioner resonant frequency is calculated by using the following equation:

$$f = \frac{1}{2\pi} \left(\frac{K}{M} \right)^{0.5} \quad (68)$$

$$K = K_{in} = 2K_{in1} \quad (69)$$

4.3. Validation of Formed Analytical Model

The first natural frequency based on the analytical method was verified through finite element analysis (FEA). The calculated result of the first natural frequency based on an analytical method was 391.91 Hz. Initially, to verify the analytical result, a 3D model of the stage was constructed using a coarse mesh. Subsequently, the model's mesh was refined

at the right circular hinges to enhance computation precision, as depicted in Figure 15. In addition, the Skewness criterion was exploited to assess the mesh quality, which indicated that the obtained outcome of a medium value was 0.49889, as shown in Figure 16. This value guarantees the attainment of a high-quality mesh for the simulation procedure of the developed positioner. The obtained outcome utilizing the FEM method demonstrated that the initial natural frequency was determined to be 386.78 Hz, as depicted in Figure 17.

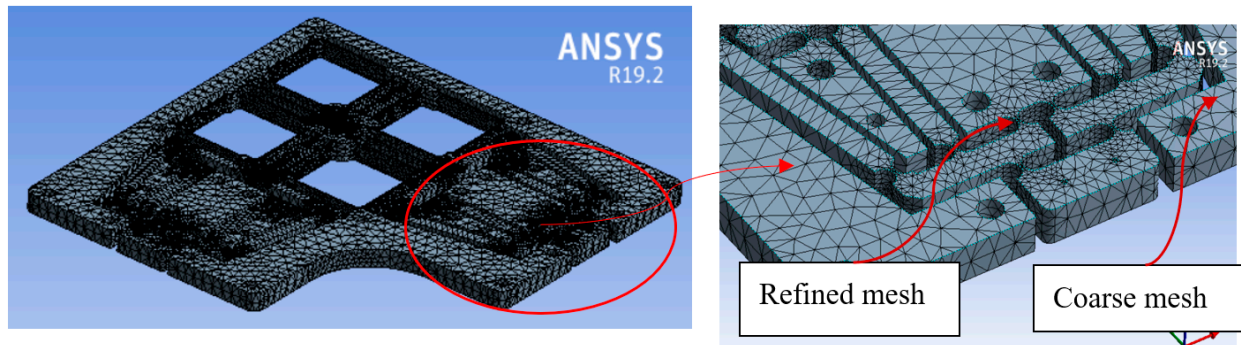


Figure 15. Meshing model for proposed positioner.

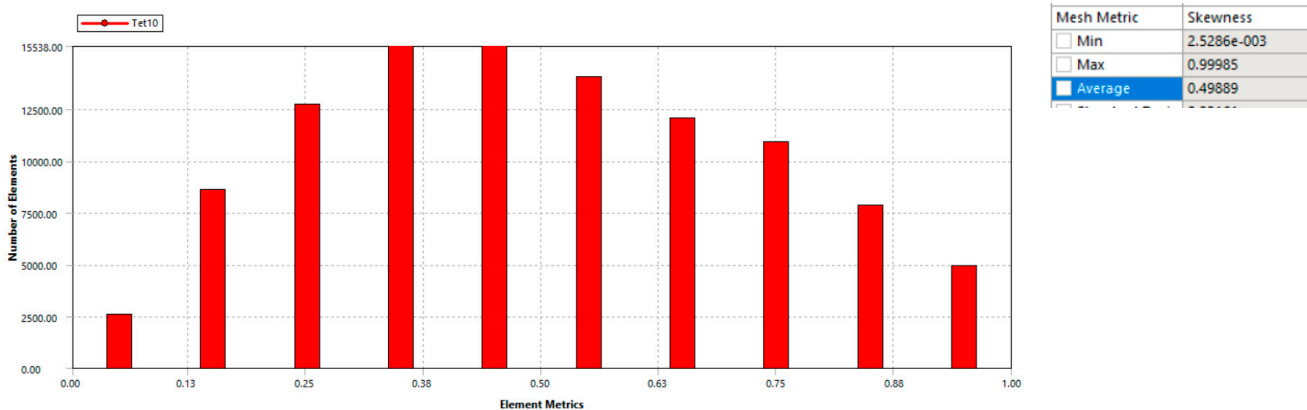


Figure 16. Skewness standard for the meshing quality of the proposed platform.

In addition, the error between the analytical method and the FEA method was 1.3%, as illustrated in Table 2. The achieved error shows that the proposed analytical method based on kinetostatic analysis is beneficial as well as reliable for quickly assessing the primary quality response of the proposed positioner.

Table 2. Verification of the analytical outcome and finite element analysis (FEA) outcome.

Response	Analytical Analysis	FEA	Error (%)
f (Hz)	391.91	386.78	1.3

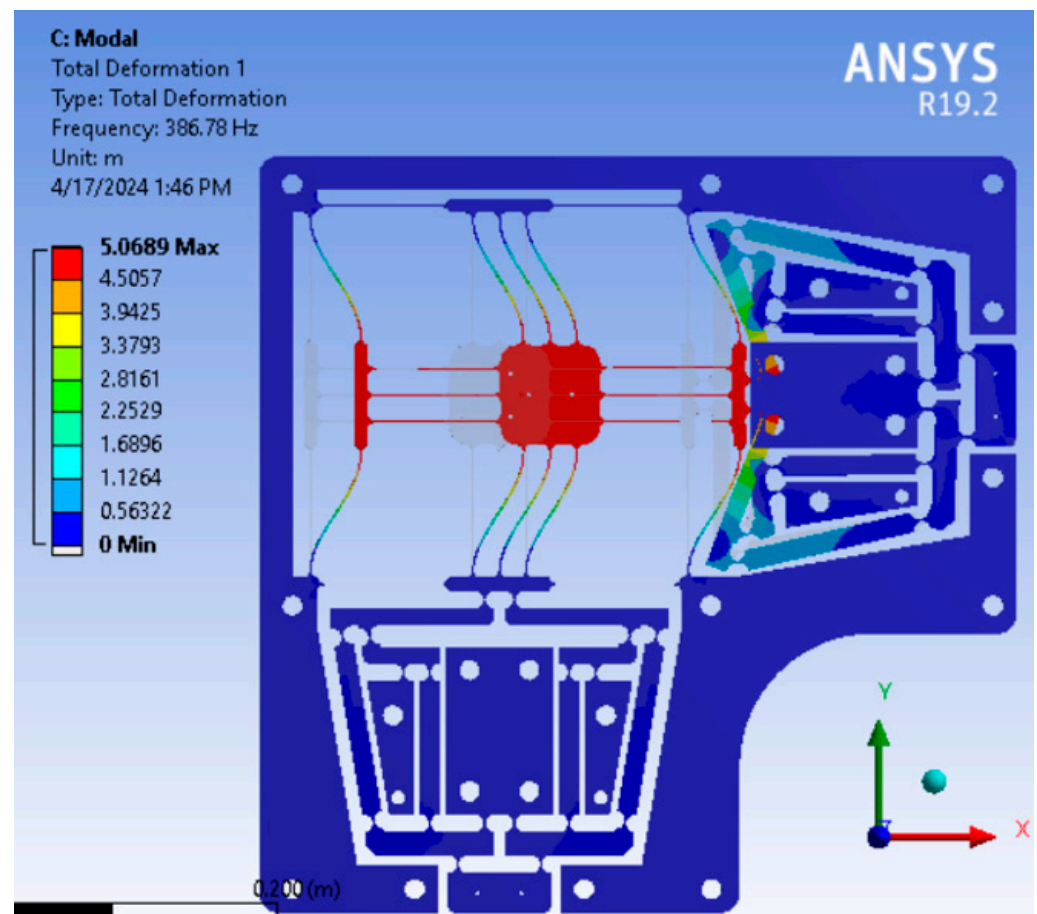


Figure 17. The first natural frequency of the initial design.

4.4. Calculation of Parasitic Motion Error for the Proposed Stage

Simultaneously, as the advanced positioner traversed in the Y-direction, a corresponding motion was seen according to the X-direction. The unintended displacement along the X-direction could be mentioned as a decoupling mobility error. According to the numerical simulation findings, the analysis showed that the parasitic motion error was extremely minimal, measuring just 0.00217% (less than 1%), as demonstrated in Table 3.

It can be inferred that the decoupling mobility error has minimal impact on the accuracy of output displacement. Additionally, the developed positioner demonstrates a strong linear connection between input displacement and output displacement, making it suitable for precise positioning control in both precise positioning systems and nanoindentation testing positioning systems. The definition of decoupling mobility error is as in the following equation:

$$e = \frac{X}{Y} 100\% \quad (70)$$

The symbol “*e*” symbolizes the decoupling mobility error, whereas “*X*” and “*Y*” signify the output deformations according to the X-direction and Y-direction, congruently.

Table 3. Outcomes of input displacement and output displacement as well as decoupling mobility error.

No.	Input Deformation (μm)	Output Deformation (Y-Direction) (μm)	Output Deformation (X-Direction) (μm)	Decoupling Mobility Error (%)
1	2	-12.585	-2.73×10^{-4}	0.002169805
2	4	-25.17	-5.46×10^{-4}	0.002169766
3	6	-37.756	-8.19×10^{-4}	0.002169695
4	8	-50.341	-1.09×10^{-3}	0.002169802
5	10	-62.926	-1.37×10^{-3}	0.002169691
6	12	-75.511	-1.64×10^{-3}	0.00216975
7	14	-88.096	-1.91×10^{-3}	0.002169792
8	16	-100.68	-2.18×10^{-3}	0.002169746
9	18	-113.27	-2.46×10^{-3}	0.002169683
10	20	-125.85	-2.73×10^{-3}	0.002169805
11	22	-138.44	-3.00×10^{-3}	0.002169749
12	24	-151.02	-3.28×10^{-3}	0.002169779
13	26	-163.61	-3.55×10^{-3}	0.002169733
14	28	-176.19	-3.82×10^{-3}	0.002169817
15	30	-188.78	-4.10×10^{-3}	0.002169721
16	32	-201.36	-4.37×10^{-3}	0.002169746
17	34	-213.95	-4.64×10^{-3}	0.002169713
18	36	-226.53	-4.92×10^{-3}	0.002169779

4.5. Parameter Optimization of Proposed XY Positioner

The initial natural frequency modes were adjusted to be very small or large to prevent resonance issues between the motors, PEA actuators, and the proposed compliant XY positioner. The initial resonance frequency was determined using the kinetostatic analysis method to assess the performance of the suggested positioner and confirm its structural integrity, as validated by the FEA analysis. In addition, to achieve high output displacement for the purpose of expanding a large working stroke and ensuring material strength with a high safety factor, the key factors of the proposed positioner of the proposed stage should be optimized to enhance the quality responses. More specifically, the optimal trouble aims to maximize the output displacement and safety factor, simultaneously.

In the computational optimization process, the two quality responses of the positioner include a safety factor, and the output deformation along the y -axis. These are considered to reach specific requirements, such as the following: (1) a great safety factor, F_1 , is required for ensuring the endurance to operate within an elastic region without failure of the developed positioner; and (2) a large output displacement, F_2 , can generate significant linear output displacement to reach a large stroke. Specifically, the multiple-objective optimization statement in this research is briefly presented as follows:

Determine design variables: $X = [K, M, H, Q, L]$

Maximize the safety factor:

$$F_1(K, M, H, Q, L) \geq 2, \quad (71)$$

Maximize the output displacement:

$$F_2(K, M, H, Q, L) \geq 240 \text{ } (\mu\text{m}), \quad (72)$$

Constraint:

$$\text{First natural frequency} > 320 \text{ Hz} \quad (73)$$

Ranges of main parameters:

$$0.62 \text{ mm} \leq H \leq 0.74 \text{ mm}, \quad (74)$$

$$7.2 \text{ mm} \leq Q \leq 12 \text{ mm}, \quad (75)$$

$$0.5 \text{ mm} \leq K \leq 0.6 \text{ mm}. \quad (76)$$

$$15 \text{ mm} \leq L \leq 18 \text{ mm}. \quad (77)$$

$$0.5 \text{ mm} \leq M \leq 0.6 \text{ mm}. \quad (78)$$

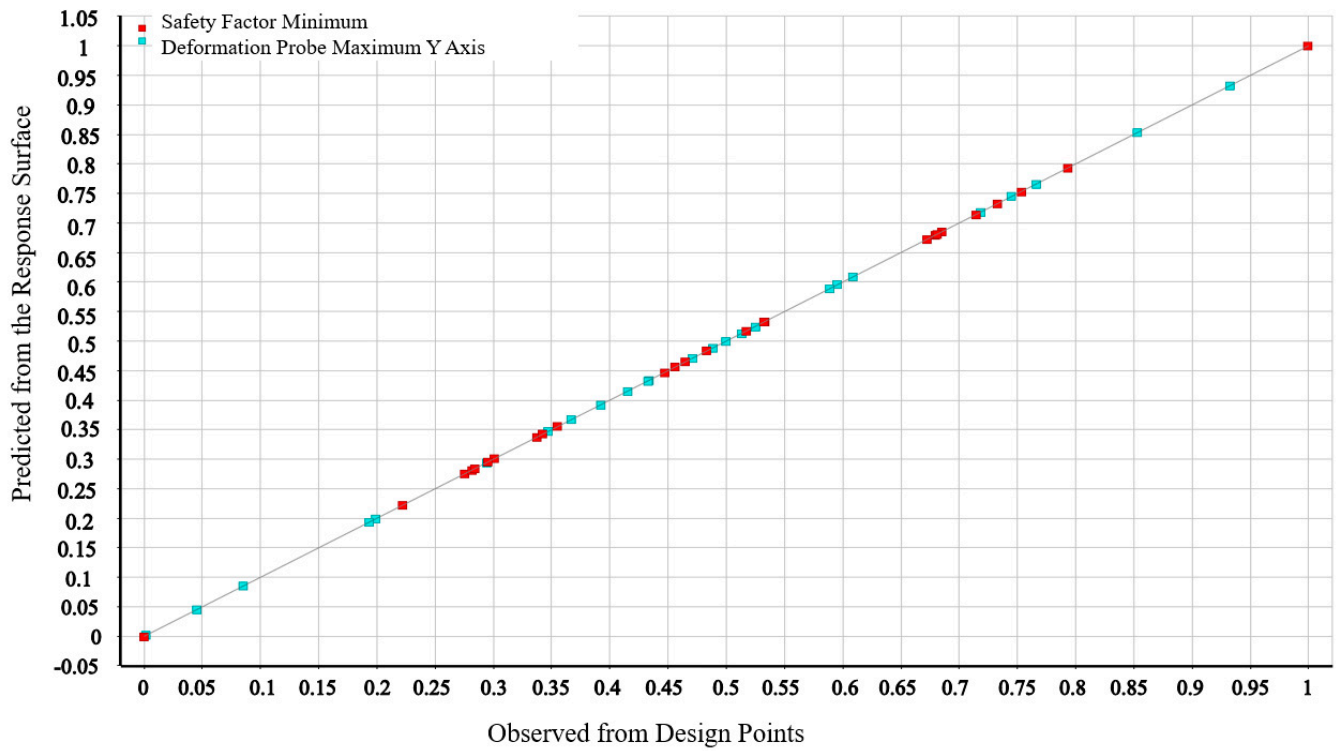
4.5.1. Establishment of Numerical Experiment Data Based on the Response Surface Method

This work used the central composite design (CCD) to construct a numerical experiment data set for the proposed positioner and to establish quantitative information. The numerical findings obtained from this stage are presented in Table 4.

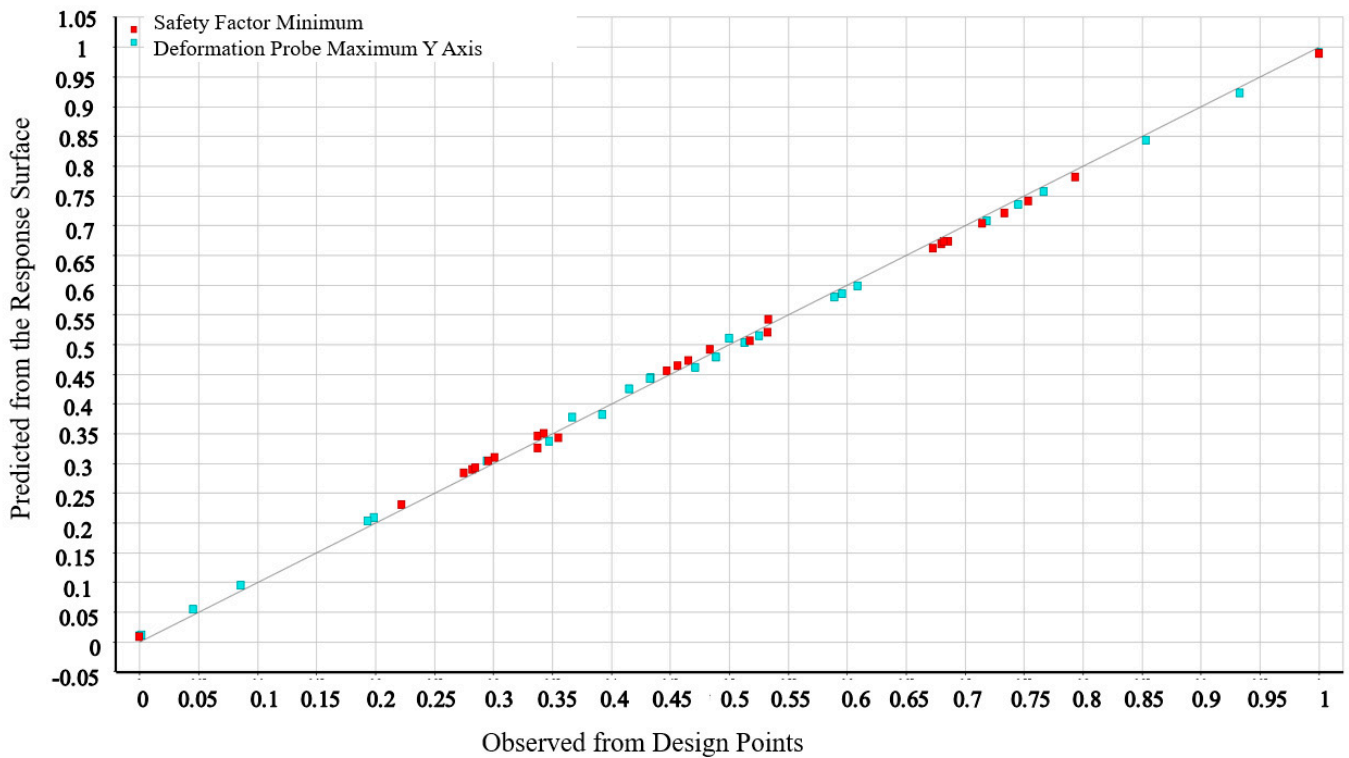
Table 4. Experimental design data points and computational outcomes.

No.	K (mm)	M (mm)	H (mm)	Q (mm)	L (mm)	Safety Factor (F ₁)	Output Displacement (F ₂) (μm)
1	0.59	0.55	0.68	9.6	16.5	2.470306	−227.048
2	0.53	0.55	0.68	9.6	16.5	2.469848	−229.74
3	0.65	0.55	0.68	9.6	16.5	2.422369	−223.184
4	0.59	0.5	0.68	9.6	16.5	2.459544	−232.922
5	0.59	0.6	0.68	9.6	16.5	2.332124	−216.928
6	0.59	0.55	0.62	9.6	16.5	2.306505	−226.276
7	0.59	0.55	0.74	9.6	16.5	2.409697	−225.984
8	0.59	0.55	0.68	7.2	16.5	2.093905	−223.396
9	0.59	0.55	0.68	12	16.5	2.800037	−223.495
10	0.59	0.55	0.68	9.6	15	2.416056	−232.89
11	0.59	0.55	0.68	9.6	18	2.435406	−219.271
12	0.573	0.535833	0.663	8.919985	16.92501	2.302705	−227.368
13	0.607	0.535833	0.663	8.919985	16.07499	2.332288	−229.829
14	0.573	0.564167	0.663	8.919985	16.07499	2.250798	−226.645
15	0.607	0.564167	0.663	8.919985	16.92501	2.288336	−218.001
16	0.573	0.535833	0.697	8.919985	16.07499	2.33591	−232.195
17	0.607	0.535833	0.697	8.919985	16.92501	2.29305	−224.523
18	0.573	0.564167	0.697	8.919985	16.92501	2.294966	−221.429
19	0.607	0.564167	0.697	8.919985	16.07499	2.344968	−225.998
20	0.573	0.535833	0.663	10.28001	16.07499	2.577991	−231.552
21	0.607	0.535833	0.663	10.28001	16.92501	2.625953	−225.102
22	0.573	0.564167	0.663	10.28001	16.92501	2.59868	−221.001
23	0.607	0.564167	0.663	10.28001	16.07499	2.574061	−224.923
24	0.573	0.535833	0.697	10.28001	16.92501	2.654309	−228.208
25	0.607	0.535833	0.697	10.28001	16.07499	2.575252	−225.386
26	0.573	0.564167	0.697	10.28001	16.07499	2.569094	−224.713
27	0.607	0.564167	0.697	10.28001	16.92501	2.611664	−220.66

To choose the suitable kind of fit diagram for mapping input parameters and quality responses, four kinds of response surface methods were investigated to find the best-fit diagram for the proposed stage. The achieved results show that the response surface Kriging had the best goodness of fit for mapping key design variables and the output characteristics of the developed positioner, as illustrated in Figure 18a–d.

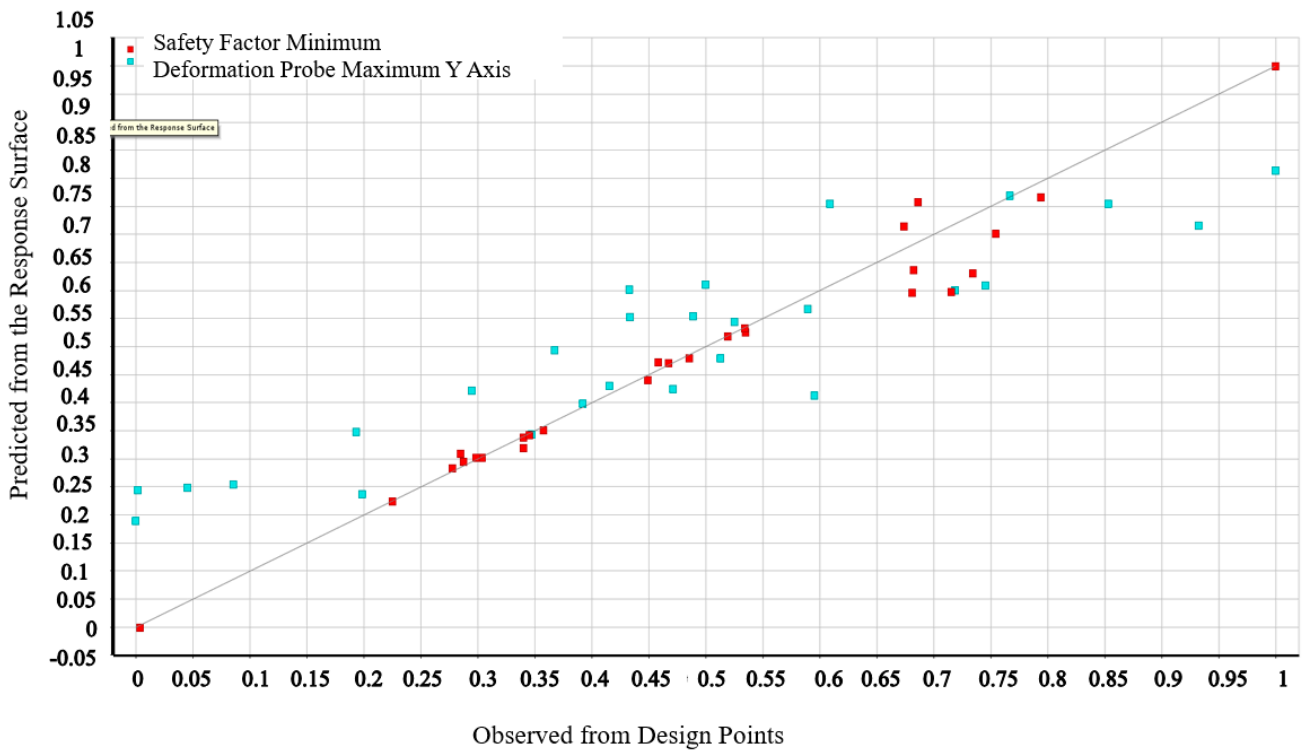


(a) Kriging

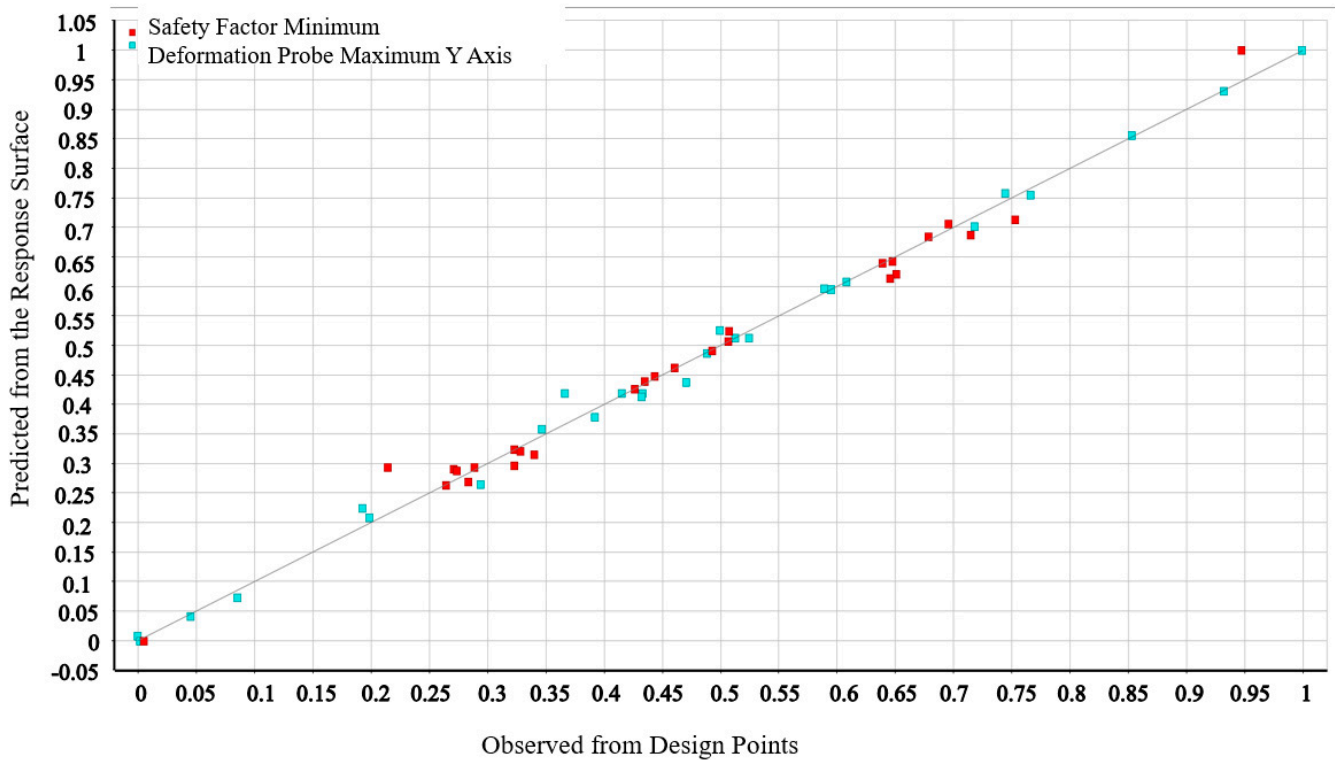


(b) Non-parametric regression

Figure 18. Cont.



(c) Neural network



(d) Standard response surface—full 2nd-order polynomials

Figure 18. Diagram of the goodness of fit for mapping among main input parameters and output characteristics based on four response surface types.

4.5.2. Optimal Result

Initially, the limitations of the developed positioner were defined, and then the most favorable procedure was executed. If the identified candidates were unable to meet the requirements of the objective function, it became necessary to revise the restrictions in order to obtain three suitable candidates that could adapt to the objective function. Table 5 displays the suggested appropriate limitations of the input variables.

Table 5. Bounds of the response surfaces.

Characteristics	Constraint Type	Lower	Upper	Unit
Maximize safety factor	Values \geq Lower	2		
Maximize output displacement	Values \geq Lower	240		(μm)

Table 6 displays three prospective candidates for the positioner, which were found based on the NSGA-II algorithm integrated in Ansys Workbench. Based on the information provided in Table 6, the third candidate was selected as the most suitable design because it successfully met the design criteria, including a safety factor greater than 2 and an output displacement exceeding 248.9 μm . Furthermore, the initial resonance frequency, determined by the ideal design variables, exceeded 320 Hz.

Table 6. Comparison among candidates.

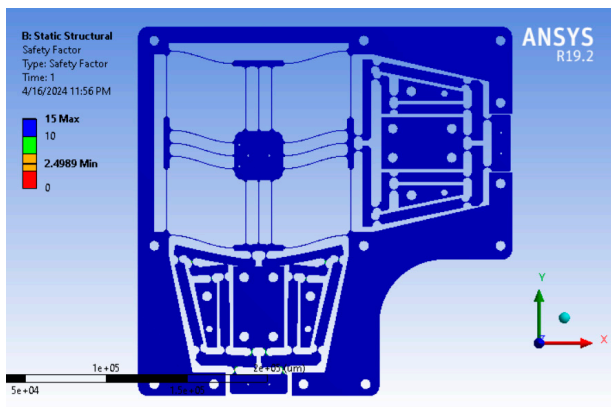
Input Parameters and Output Responses	Candidate Point 1	Candidate Point 2	Candidate Point 3
M (mm)	0.53015	0.53059	0.53045
K (mm)	0.50012	0.50018	0.50048
H (mm)	0.6398	0.62673	0.63099
Q (mm)	11.932	10.407	10.293
L (mm)	17.859	16.045	15.492
Safety Factor (F_1)	3.1448	2.4922	2.4025
Output displacement F_2 (μm)	248.24	248.24	248.9

4.5.3. FEA Validation

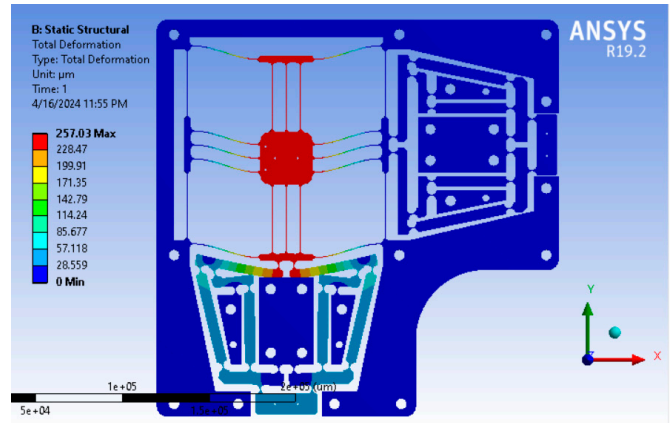
The 3D model of the positioner for FEA analysis was constructed using the optimal parameters of the third candidate. The method was executed with identical input displacement and fixed limitations. The achieved results show that the output displacement (Y -direction) was 242.16 μm and the safety factor was 2.4989, as illustrated in Figure 19a. In addition, the whole displacement was 257.03 μm , as portrayed in Figure 19b. Table 7 demonstrates that the discrepancy between the ideal outcome and the FEA analysis was rather minor. The output displacement had an error of 2.78% and the safety factor had an error of 3.86%. The comparison results indicate that the hybrid technique, which combines the response surface method, NSGA-II, and FEM, is a very effective and reliable way to approximate the relationship between inputs and outputs in order to optimize the multi-objective problem of the constructed positioner. In addition, the optimal natural frequencies of fix modes of the proposed stage based on FEA analysis were 371.83 Hz, 373.28 Hz, 899.52 Hz, 945.68 Hz, 1211.3 Hz, and 1226.2 Hz, respectively, as illustrated in Figure 20.

Table 7. Observed discrepancy between optimal consequence of RSM and FEA consequence.

Attribute	Optimized Consequence Based on RSM	FEA Consequence	Discrepancy (%)
F_1	2.4025	2.4989	3.86
F_2 (μm)	248.9	242.16	2.78

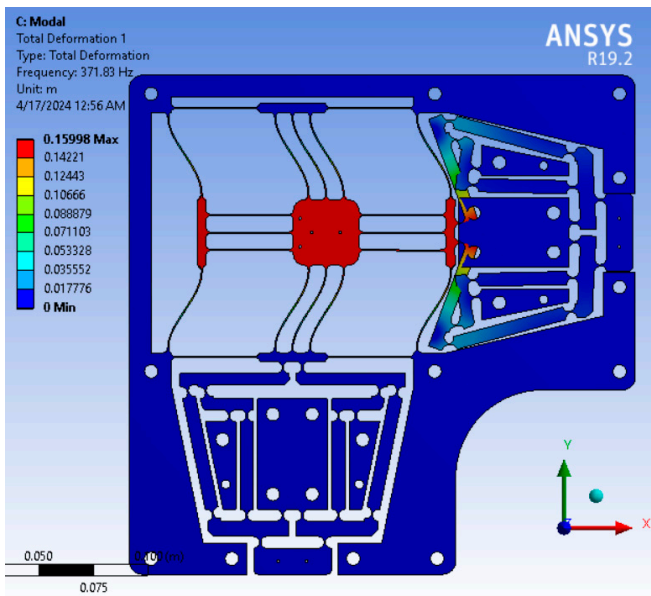


(a) Safety factor

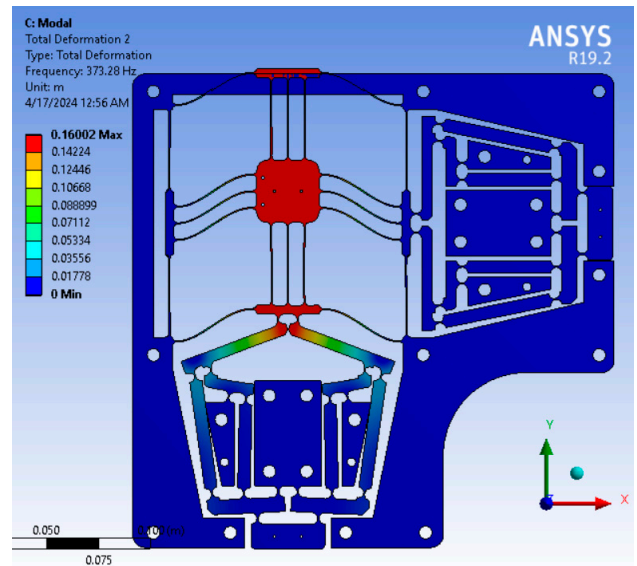


(b) Total deformation

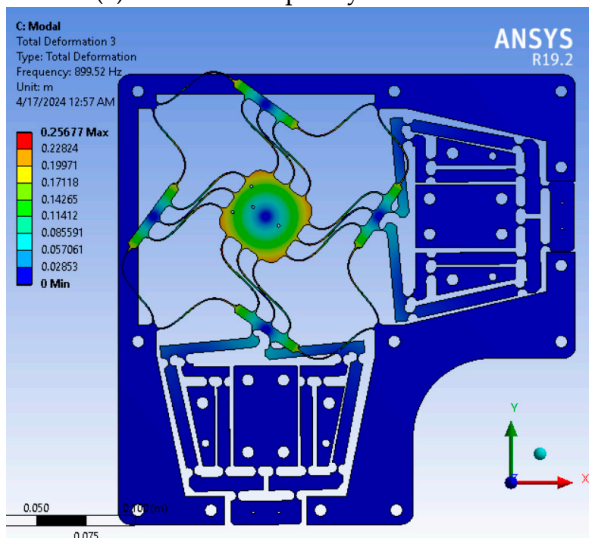
Figure 19. FEA analysis results: (a) safety factor, (b) total deformation.



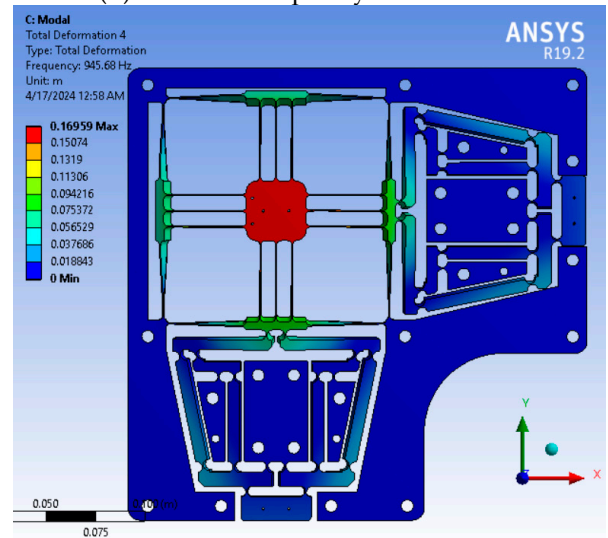
(a) Resonant frequency of 1st mode



(b) Resonant frequency of 2nd mode



(c) Resonant frequency of 3rd mode



(d) Resonant frequency of 4th mode

Figure 20. Cont.

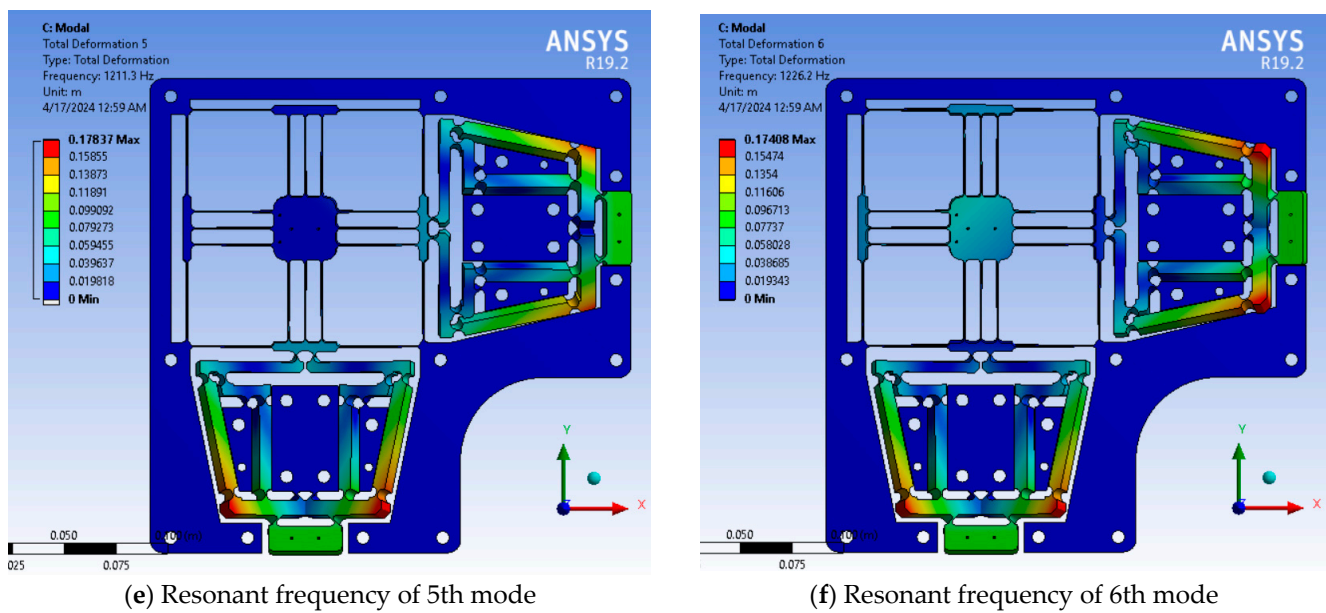


Figure 20. Resonant frequencies of six modes based on FEM analysis.

4.6. Experimental Study

4.6.1. Prototype Fabrication

To validate the output attributes of the proposed structure, a prototype of the developed positioner was manufactured with an alloy material, AL-7075. Unlike previous studies that applied the wire electric discharge machining process method to fabricate the compliant positioning stage, this study applied a computerized numerical control milling process with a small endmill tool to fabricate the proposed prototype so as to enhance the fabrication accuracy as well as the quality of the manufactured surfaces. The manufactured prototype and device layout for measuring the quality responses of the proposed positioner are illustrated in Figure 21. The key factors of geometrical dimensions for the stage are depicted in Table 1. The proposed positioner had total dimensions of 228 mm × 228 mm × 10 mm.

The compliant positioner was operated based on two PEAs (piezoelectric actuator) (model PI 225.10, PI Company, Karlsruhe, Germany), with a maximum output stroke of 15 μm. In addition, the output displacement was measured by two laser displacement sensors with a precision of 0.05 μm (model LK-G30, Keyence Company, Osaka, Japan).

4.6.2. Experimental Results and Discussion

The experimental setup, illustrated in Figure 21, was intended to measure the first natural response of the proposed hammer test method. The LK-G30 laser displacement sensor, produced by the Keyence company in Japan, precisely detected the vibration of the central platform in the X and Y directions with a precision of 0.05 μm. To be specific, this study used the LK-G30 laser displacement sensor to capture the signals to record data using controlled software for the laser displacement sensor, as illustrated in Figure 22. Afterwards, the gathered data were analyzed using the fast Fourier transform algorithm implemented into Matlab R2021b to determine the first natural frequency.

To validate the first natural response of the proposed positioner, the simulated result of the frequency of the stage based on Ansys software R19.2 achieved 371.83 Hz. Then, the proposed design was fabricated using the computerized numerical control milling method so as to reach the high-quality surface of the prototype. Furthermore, the natural frequency result of the experiment achieved at the first peak was 329.59 Hz, as illustrated in Figure 23. Finally, the error between the FEA result and the experimental result was 11.36%, as illustrated in Table 8. The achieved error result shows that the measured natural frequency of the positioning system was relatively close to the FEA result.

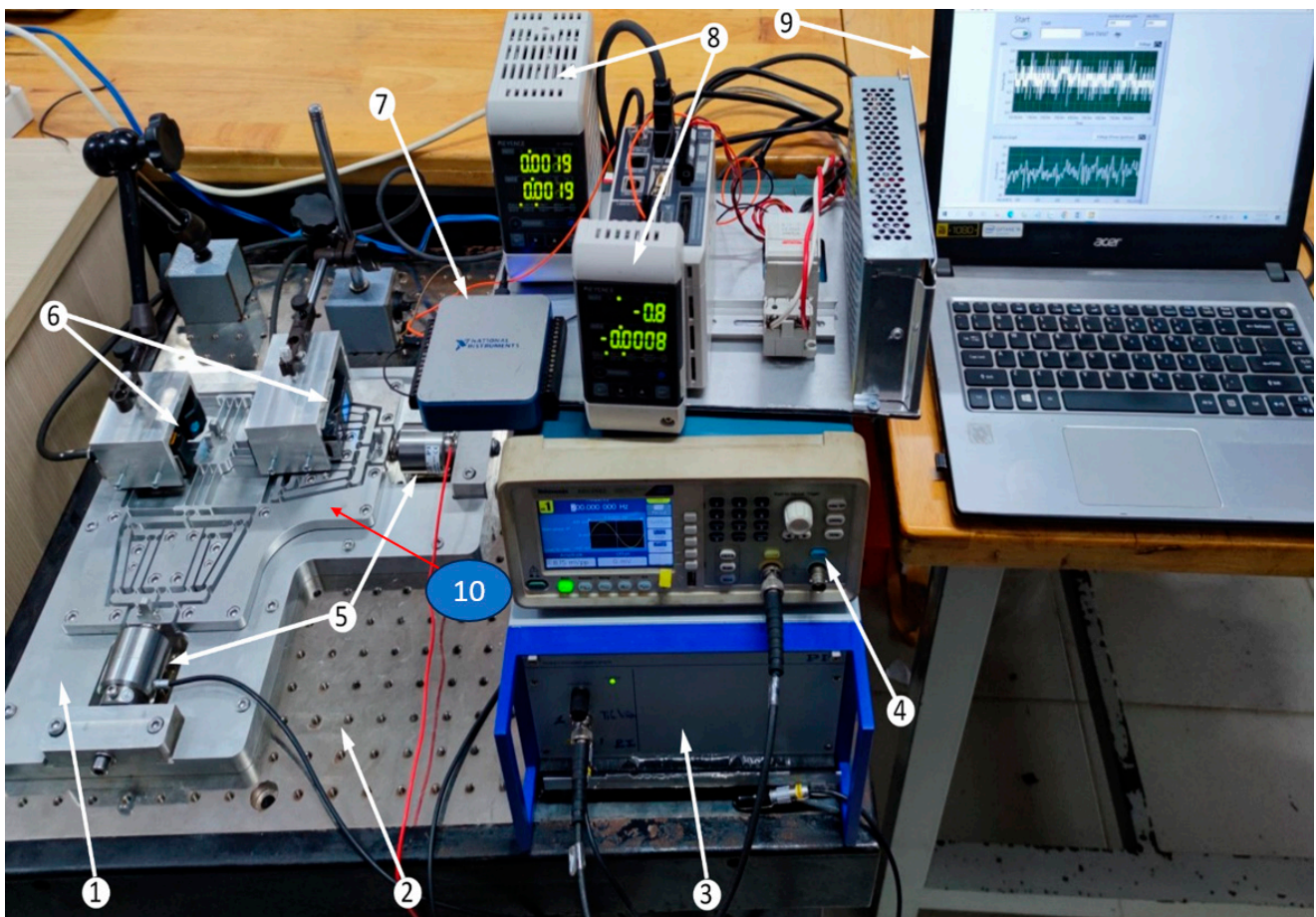


Figure 21. Experimental setup to measure output responses. (1) Intermediate plate; (2) vibration-isolated table; (3) PI driver; (4) pulse generator; (5) PEA; (6) displacement laser sensor; (7) National Instrument Card; (8) controller LK for laser sensor; (9) computer; and (10) developed XY positioner.

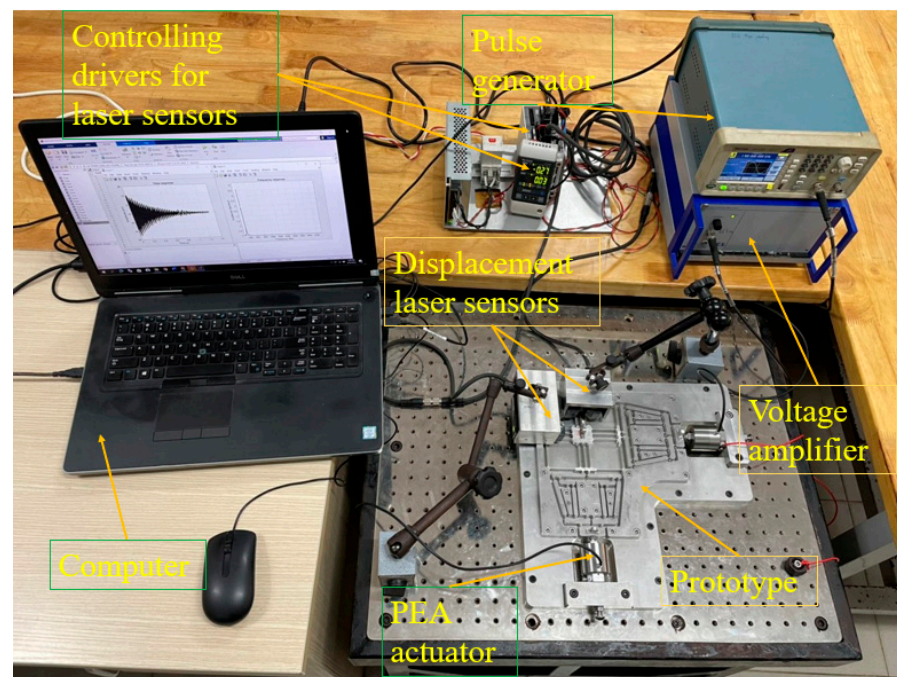


Figure 22. Experimental setup to measure the first natural frequency.

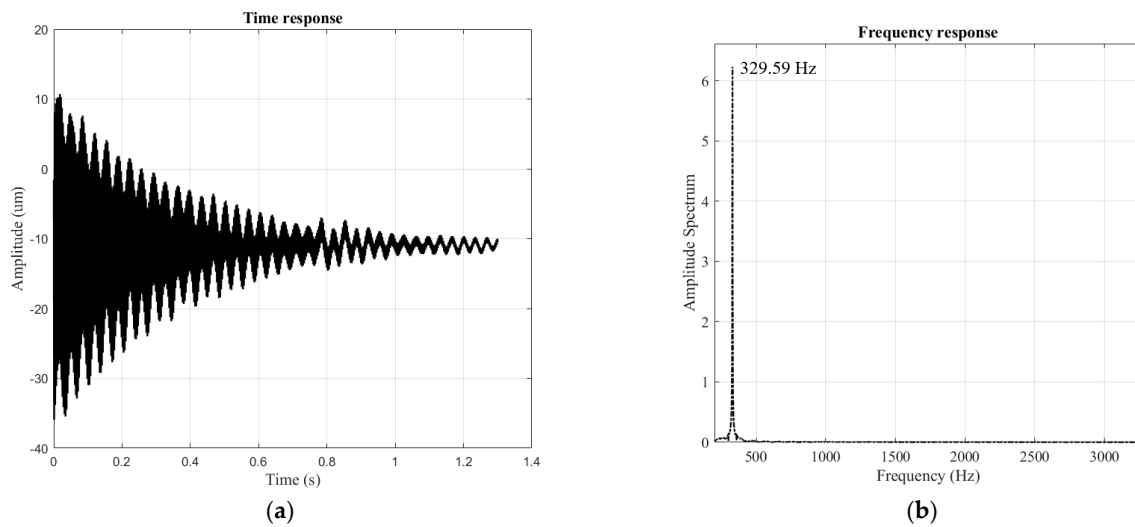


Figure 23. Dynamic responses of the proposed positioner: (a) time response, (b) first natural response measured through experimental testing.

Table 8. Validation of the simulation result and experimental result.

Response	Simulation	Experiment	Error (%)
f (Hz)	371.83	329.59	11.36 (%)

In addition, due to the limitation of displacement of PEA, translational screws combined with displacement sensors were utilized to investigate the input displacement and output displacement of fabricated prototype. The experimental layout of the measuring instruments is illustrated in Figure 24. Specifically, input displacement and output displacement of the experimental results were measured five times, and average values were calculated. The linear relationships of input displacement and output displacement were achieved by FEA and experiment results, as demonstrated in Figure 25. The result shows that the proposed structure achieved a good linear relationship for the input displacement and output displacement.

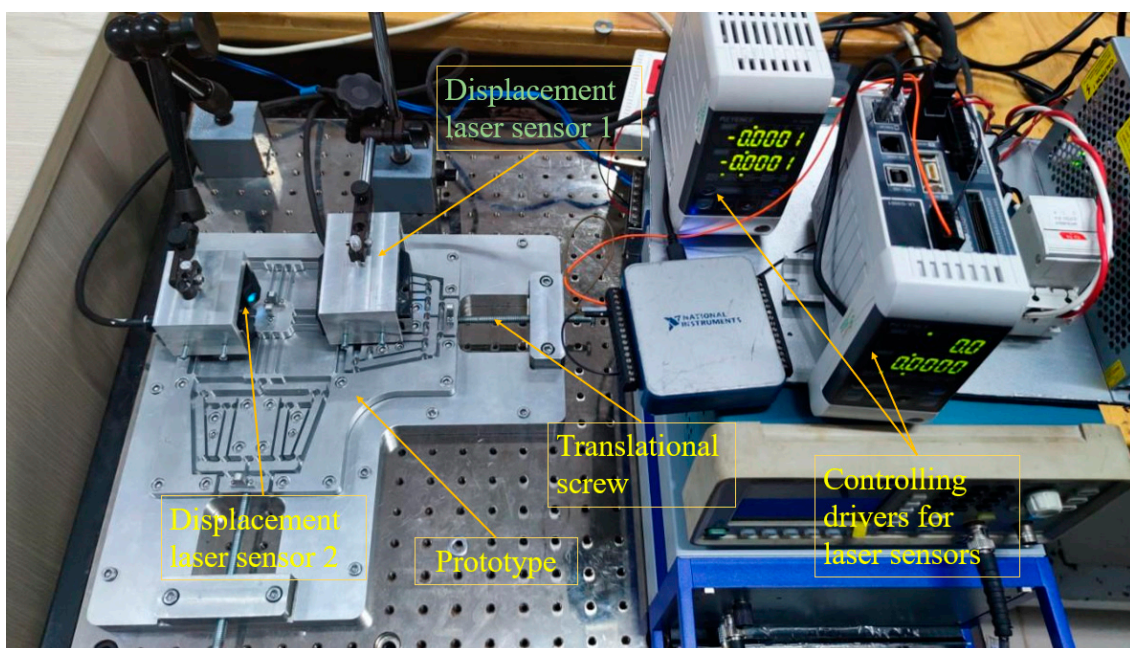


Figure 24. Measuring mechanism displacement using a translational screw.

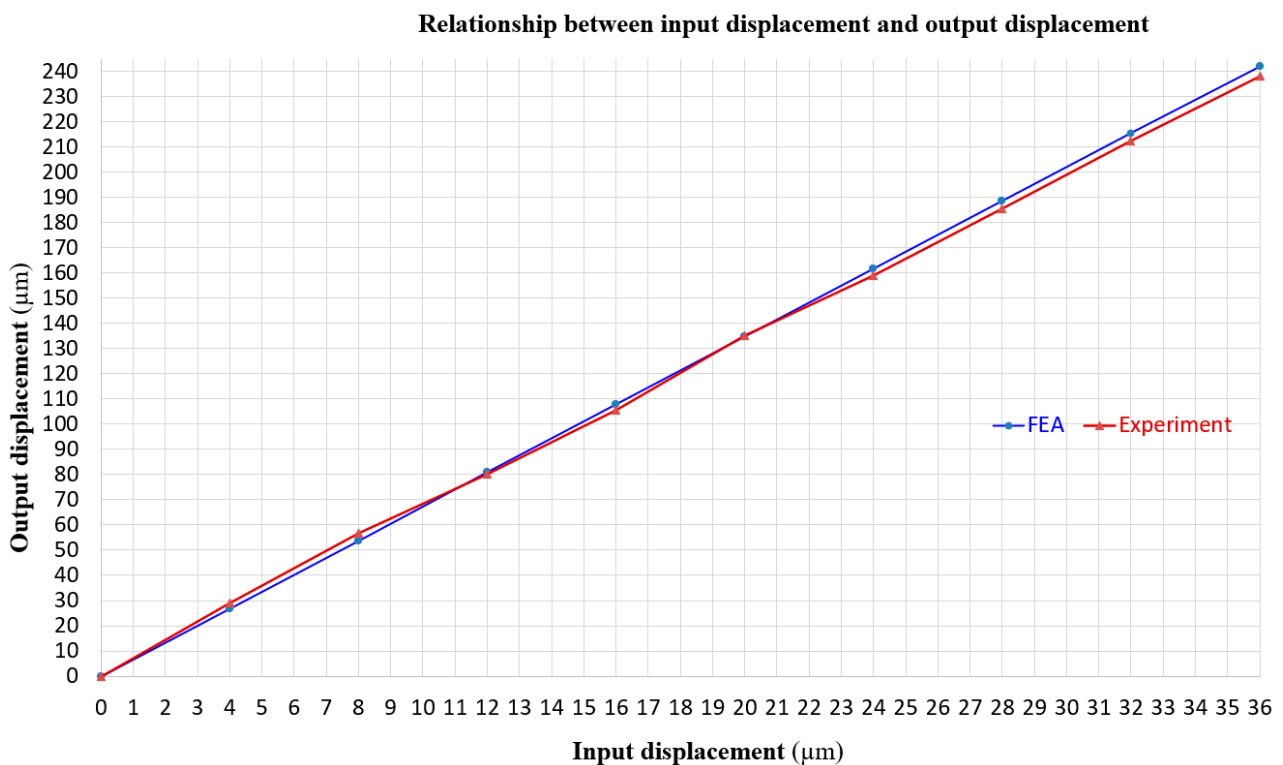


Figure 25. Diagram of the relationship between input displacement and output displacement.

5. Conclusions

In this research, a novel compliant XY positioner was proposed based on an advanced six-lever displacement amplifier arranged at an inclination angle of the rigid bar integrated right circular hinges. This positioner also utilizes a parallel guiding mechanism integrated with flexure leaf hinges. The ultimate goals are to attain a compact structure, high first natural frequency, relatively good linear motion, and large displacement intensification proportion, as well as to reduce the decoupling mobility error.

First of all, to quickly evaluate the initial quality response, a combination method of kinetostatic analysis, the Lagrange method, and FEA analysis was applied to determine and verify the quality characteristics of the stage. The experiment result shows that the error between the analytical and FEA methods was 1.3%. In addition, the parasitic motion error of the proposed stage was relatively small with 0.00217. This achieved error ensures precise position control for positioning in a precise positioning system and nanoindentation testing system.

Moreover, to further improve the quality attributes of the suggested positioner, a combination of the response surface method and NSGA-II algorithm was utilized to achieve the optimal design variables. The attained optimization results found three potential candidates satisfactory for the aforementioned requirements, and the third candidate was chosen according to the benefits of high output displacement and the satisfaction of the requirements of quality responses, such as first natural frequency and safety factor. The optimal parameter dimensions of the third candidate were found at $M = 0.53045$ mm, $K = 0.50048$ mm, $H = 0.63099$ mm, $Q = 10.293$, and $L = 15.492$ mm, and the optimal results of the safety factor and output displacement were 2.4025 and 248.9 μm. In addition, the FEA verification findings indicated that the safety factor was 2.4989, and the output displacement was 242.16 μm. The discrepancies between the optimized and FEA results were 3.86% and 2.78%, respectively.

Ultimately, a prototype of the proposed positioner was manufactured based on the CNC milling method and measurement of the first natural frequency. The relationship between input displacement and output displacement was assessed to validate the ex-

perimental results and FEA results. The FEA result and experimental result of the first resonant frequency were 329.59 Hz and 371.83 Hz, respectively, and the error between the FEA result and experimental result for the first resonant frequency was 11.36%. In addition, the results show that the relationship between the experimental result's input and output displacement and the developed structure's FEA result achieved a good linear connection. Therefore, the proposed positioner can be considered as a potential configure applied in an accurate positioning system and a nanoindentation testing positioning system for checking bio-specimens' behaviors.

In future works, a new design structure with good characteristics will be developed for positioning in a precise positioning system and nanoindentation testing system.

Author Contributions: Conceptualization, M.P.D.; methodology, M.P.D. and H.G.L.; software, M.P.D. and V.D.T.N.; validation, M.P.D. and H.G.L.; formal analysis, N.L.C.; investigation, C.T.T. and V.D.T.N.; data curation, M.P.D. and V.D.T.N.; writing—original draft preparation, M.P.D.; writing—review and editing, M.P.D. and N.L.C. All authors have read and agreed to the published version of the manuscript.

Funding: This work belongs to the project grant No: T2023-124. funded by Ho Chi Minh City University of Technology and Education, Vietnam.

Data Availability Statement: Data are contained within the article.

Conflicts of Interest: The authors declare that they have no known competing financial interests or personal relationships that could have appeared to influence the work reported in this paper.

Nomenclature

1-dof	One degree of freedom
2-dof	Two degrees of freedom
TM	Taguchi method
RSM	Response surface methodology
ASDA	Advanced six-lever displacement amplifier
PEA	Piezoelectric actuator
LAM	Lever displacement amplifier
FEA	Finite element analysis
FEM	Finite element method
NSGA-II	Nondominated Sorting Genetic Algorithm II
f	First natural frequency
K_B^{rc}	The bending rigidity of right circular hinge
K_T^{rc}	The rotation rigidity of right circular hinge
K_L^{rc}	Linear stiffness of right circular hinge
CCD	Central composite design
K_T^l	The rotation rigidity of leaf hinge
K_L^l	Linear stiffness of leaf hinge

References

- Hu, Z.; Lynne, K.J.; Markondapatnaikuni, S.P.; Delfanian, F. Material elastic–plastic property characterization by nanoindentation testing coupled with computer modeling. *Mater. Sci. Eng. A* **2013**, *587*, 268–282. [\[CrossRef\]](#)
- Nowak, J.D.; Rzepiejewska-Malyska, K.A.; Major, R.C.; Warren, O.L.; Michler, J. In-situ nanoindentation in the SEM. *Mater. Today* **2010**, *12*, 44–45. [\[CrossRef\]](#)
- Guo, Z.; Ma, T.; Yang, X.; Li, J.; Li, W.; Vairis, A. Multi-scale analyses of phase transformation mechanisms and hardness in linear friction welded Ti17 ($\alpha + \beta$)/Ti17 (β) dissimilar titanium alloy joint. *Chin. J. Aeronaut.* **2024**, *37*, 312–324. [\[CrossRef\]](#)
- Alderete, N.; Zaheri, A.; Espinosa, H.D. A novel in situ experiment to investigate wear mechanisms in biomaterials. *Exp. Mech.* **2019**, *59*, 659–667. [\[CrossRef\]](#)
- Howell, L.L.; Magleby, S.P.; Olsen, B.M.; Wiley, J. (Eds.) *Handbook of Compliant Mechanisms*; John Wiley & Sons, Incorporated: New York, NY, USA, 2013.
- Song, B.; Zhang, D.; Jing, X.; Ren, Y.; Chen, Y.; Li, H. Theoretical and Experimental Investigation of Surface Textures in Vibration-Assisted Micro Milling. *Micromachines* **2024**, *15*, 139. [\[CrossRef\]](#)
- Rashed, E.O.; Nofal, A.; Abd El-Malek, A.H.; Hossam, M. Development of a Two-Dimensional Ultrasonic Device for Vibration-Assisted Milling. *Machines* **2022**, *10*, 362. [\[CrossRef\]](#)

8. Dang, M.P.; Le, H.G.; Le, N.N.T.; Le Chau, N.; Dao, T.P. Multiresponse optimization for a novel compliant Z-stage by a hybridization of response surface method and whale optimization algorithm. *Math. Probl. Eng.* **2021**, *2021*, 9974230. Available online: <https://onlinelibrary.wiley.com/doi/epdf/10.1155/2021/9974230> (accessed on 12 June 2024). [\[CrossRef\]](#)
9. Rabe, R.; Breguet, J.M.; Schwaller, P.; Stauss, S.; Haug, F.J.; Patscheider, J.; Michler, J. Observation of fracture and plastic deformation during indentation and scratching inside the scanning electron microscope. *Thin Solid Film.* **2004**, *469*, 206–213. [\[CrossRef\]](#)
10. Huang, H.; Zhao, H.; Mi, J.; Yang, J.; Wan, S.; Xu, L.; Ma, Z. A novel and compact nanoindentation device for in situ nanoindentation tests inside the scanning electron microscope. *Aip Adv.* **2012**, *2*, 012104. [\[CrossRef\]](#)
11. Huang, H.; Zhao, H.; Shi, C.; Hu, X.; Cui, T.; Tian, Y. A tension stress loading unit designed for characterizing indentation response of single crystal silicon under tension stress. *AIP Adv.* **2013**, *3*, 092125. [\[CrossRef\]](#)
12. Dang, M.P.; Le, H.G.; Tran, N.T.D.; Chau, N.L.; Dao, T.P. Optimal design and analysis for a new 1-DOF compliant stage based on additive manufacturing method for testing medical specimens. *Symmetry* **2022**, *14*, 1234. [\[CrossRef\]](#)
13. Huang, H.; Zhao, H.; Mi, J.; Yang, J.; Wan, S.; Yang, Z.; Geng, C. Experimental research on a modular miniaturization nanoindentation device. *Rev. Sci. Instrum.* **2011**, *82*, 095101. [\[CrossRef\]](#)
14. Li, J.; Huang, H.; Morita, T. Stepping piezoelectric actuators with large working stroke for nano-positioning systems: A review. *Sens. Actuators A Phys.* **2019**, *292*, 39–51. [\[CrossRef\]](#)
15. Kim, H.Y.; Ahn, D.H.; Gweon, D.G. Development of a novel 3-degrees of freedom flexure based positioning system. *Rev. Sci. Instrum.* **2012**, *83*, 055114. [\[CrossRef\]](#)
16. Ling, M.; Cao, J.; Jiang, Z.; Zeng, M.; Li, Q. Optimal design of a piezo-actuated 2-DOF millimeter-range monolithic flexure mechanism with a pseudo-static model. *Mech. Syst. Signal Process.* **2019**, *115*, 120–131. [\[CrossRef\]](#)
17. Dao, T.P.; Huang, S.C. Design and multi-objective optimization for a broad self-amplified 2-DOF monolithic mechanism. *Sādhanā* **2017**, *42*, 1527–1542. [\[CrossRef\]](#)
18. Yong, Y.K.; Aphale, S.S.; Moheimani, S.R. Design, identification, and control of a flexure-based XY stage for fast nanoscale positioning. *IEEE Trans. Nanotechnol.* **2008**, *8*, 46–54. [\[CrossRef\]](#)
19. Ding, B.; Li, Y. Design and analysis of a decoupled XY micro compliant parallel manipulator. In Proceedings of the 2014 IEEE International Conference on Robotics and Biomimetics (ROBIO 2014), Bali, Indonesia, 5–10 December 2014; pp. 1898–1903.
20. Zhou, S.; Yan, P. Design and Analysis of a Hybrid Displacement Amplifier Supporting a High-Performance Piezo Jet Dispenser. *Micromachines* **2023**, *14*, 322. [\[CrossRef\]](#)
21. Wu, H.; Lai, L.; Zhang, L.; Zhu, L. A novel compliant XY micro-positioning stage using bridge-type displacement amplifier embedded with Scott-Russell mechanism. *Precis. Eng.* **2022**, *73*, 284–295. [\[CrossRef\]](#)
22. Gu, Y.; Duan, X.; Lin, J.; Yi, A.; Kang, M.; Jiang, J.; Zhou, W. Design, analysis, and testing of a novel 2-DOF vibration-assisted polishing device driven by the piezoelectric actuators. *Int. J. Adv. Manuf. Technol.* **2020**, *111*, 471–493. [\[CrossRef\]](#)
23. Wu, Z.; Li, Y.; Hu, M. Design and optimization of full decoupled micro/nano-positioning stage based on mathematical calculation. *Mech. Sci.* **2018**, *9*, 417–429. [\[CrossRef\]](#)
24. Zhang, Q.; Zhao, J.; Peng, Y.; Pu, H.; Yang, Y. A novel amplification ratio model of a decoupled XY precision positioning stage combined with elastic beam theory and Castigliano's second theorem considering the exact loading force. *Mech. Syst. Signal Process.* **2020**, *136*, 106473. [\[CrossRef\]](#)
25. Zhu, W.L.; Zhu, Z.; Guo, P.; Ju, B.F. A novel hybrid actuation mechanism based XY nanopositioning stage with totally decoupled kinematics. *Mech. Syst. Signal Process.* **2018**, *99*, 747–759. [\[CrossRef\]](#)
26. Ding, B.; Li, Y.; Xiao, X.; Tang, Y.; Li, B. Design and analysis of a 3-DOF planar micromanipulation stage with large rotational displacement for micromanipulation system. *Mech. Sci.* **2017**, *8*, 117–126. [\[CrossRef\]](#)
27. Dang, M.P.; Le, H.G.; Chau, N.L.; Dao, T.P. Optimization for a flexure hinge using an effective hybrid approach of fuzzy logic and moth-flame optimization algorithm. *Math. Probl. Eng.* **2021**, *2021*, 6622655. Available online: <https://onlinelibrary.wiley.com/doi/epdf/10.1155/2021/6622655> (accessed on 12 June 2024). [\[CrossRef\]](#)
28. Dao, T.P.; Huang, S.C.; Thang, P.T. Hybrid Taguchi-cuckoo search algorithm for optimization of a compliant focus positioning platform. *Appl. Soft Comput.* **2017**, *57*, 526–538. [\[CrossRef\]](#)
29. Huang, S.C.; Dao, T.P. Multi-objective optimal design of a 2-DOF flexure-based mechanism using hybrid approach of grey-Taguchi coupled response surface methodology and entropy measurement. *Arab. J. Sci. Eng.* **2016**, *41*, 5215–5231. [\[CrossRef\]](#)
30. Murugan, P.; Kannan, S.; Baskar, S. NSGA-II algorithm for multi-objective generation expansion planning problem. *Electr. Power Syst. Res.* **2009**, *79*, 622–628. [\[CrossRef\]](#)
31. Martínez-Vargas, A.; Domínguez-Guerrero, J.; Andrade, Á.G.; Sepúlveda, R.; Montiel-Ross, O. Application of NSGA-II algorithm to the spectrum assignment problem in spectrum sharing networks. *Appl. Soft Comput.* **2016**, *39*, 188–198. [\[CrossRef\]](#)

Disclaimer/Publisher's Note: The statements, opinions and data contained in all publications are solely those of the individual author(s) and contributor(s) and not of MDPI and/or the editor(s). MDPI and/or the editor(s) disclaim responsibility for any injury to people or property resulting from any ideas, methods, instructions or products referred to in the content.